



Non-linear phase linking using joined distributed and persistent scatterers

Sara Mirzaee ^{a,*}, Falk Amelung ^a, Heresh Fattah ^b

^a Rosenstiel School of Marine and Atmospheric and Earth Science, University of Miami, Miami, FL, USA

^b Jet Propulsion Laboratory, California Institute of Technology, Pasadena, CA, USA

ARTICLE INFO

Keywords:

Phase linking
MiaplPy
Distributed scatterer
InSAR
Sequential

ABSTRACT

We describe a python package for nonlinear phase linking of full resolution SAR images using both distributed and persistent scatterers. In the workflow, the first step is to find for each pixel the set of self-similar pixels in order to identify persistent and distributed scatterers. Next the phase linking is performed using the full complex coherence matrix containing the wrapped phase values of each distributed scatterer. Our package uses a hybrid approach consisting of eigenvalue decomposition-based maximum likelihood phase linking and the classic eigenvalue decomposition method. The latter is used for pixels with a non-invertible covariance matrix. A sequential mode achieves computational efficiency. The next step is to unwrap the phase by selecting an optimum unwrapping network of interferograms and invert for the unwrapped phase time-series which is converted to the displacement time-series. We show how the performance of phase linking depends on the temporal correlation behavior using simulations of the coherence matrix. The sequential approaches better retrieve the simulated phases compared to the non-sequential approaches for all temporal coherence models. Phase linking methods retrieve the simulated phase with residuals close to the Cramér–Rao lower bound for coherent seasons where the absolute values of coherence matrix are high and provide a tool for obtaining InSAR measurements over areas with seasonal snowfall. We furthermore show that unwrapping errors propagate differently depending on the unwrapping network. For single-reference networks there is no error propagation, but for sequential networks it compromises the accuracy of the final displacement time-series. Delaunay networks provide an optimum solution in terms of accuracy and precision if there are several years of data with frequent temporal decorrelation or strong seasonal decorrelation. We present applications using Sentinel-1 data in different natural and anthropogenic environments.

1. Introduction

Interferometric Synthetic Aperture Radar (InSAR) has emerged as a tool for broad applications in different fields including but not limited to hydrology, seismology, glaciology, natural disaster monitoring and forestry by providing information about water and ice dynamics, canopy height and sub-centimetric displacements over wide areas of several kilometers (Amelung et al., 2000; Chaussard et al., 2013; Fattah and Amelung, 2016; Funning et al., 2005; Hoffmann et al., 2001; Joughin et al., 2011; Lanari et al., 2007; Motagh et al., 2017; Soja et al., 2015). Successful demonstration of the technique in the last three decades has led to operational InSAR missions such as Sentinel-1 and NISAR (to be launched in 2024).

Spatial and temporal decorrelation of the targets because of vegetation growth, moisture change, and seasonal snow coverage remains a challenge for obtaining reliable InSAR measurements (Arnold et al.,

2018; Ferretti et al., 2001; Kumar and Venkataraman, 2011). Accordingly, the radar targets are classified into two groups based on amplitude and phase stability. One group are the persistent scatterers (PS) with high signal-to-noise ratio. The second group are the distributed scatterers (DS) that show moderate temporal decorrelation compared to PS. Persistent scatterer techniques exploit strong scatterers based on amplitude stability (Ferretti et al., 2000, 2001; Colesanti et al., 2003) and/or phase dispersion criteria (Hooper et al., 2004, 2007) on a set of single-reference interferograms to obtain radar line of sight displacement velocity field. Other methods use maximum likelihood statistical tests (Shanker and Zebker, 2007; Zebker et al., 2007) to select coherent pixels based on an expected phase distribution that can find a denser network of PS pixels over natural terrain. More recently, Navneet et al. (2018) proposed to use the statistics of eigenvalues of the interferometric covariance matrix to select more reliable coherent pixels and reject noisy pixels in low coherence regions.

* Corresponding author.

E-mail address: sara.mirzaee@earth.miami.edu (S. Mirzaee).

The classic Small Baseline Subset (SBAS) method (Berardino et al., 2002; Schmidt and Bürgmann, 2003) was the pioneer algorithm to estimate InSAR time-series over DS pixels. Classic SBAS is based on small temporal and small spatial baseline interferograms to assure selecting highly coherent pixels. However, different approaches have been developed to extend the SBAS method to full resolution (Hooper, 2008; Lanari et al., 2004, 2007), identifying single look, slowly decorrelating, filtered pixels. For example, Pepe et al. (2015) proposed a two-step pre-processing approach to reduce the non-zero closure phases. The first step is to filter a redundant set of multi-looked interferograms by minimizing the circular variance between raw and the filtered wrapped phase time-series. The second step is to unwrap a set of selected interferograms based on maximizing the average coherence.

Another group of time-series analysis techniques for DS are phase linking approaches (Guarnieri & Tebaldini, 2007, 2008), which retrieve consistent wrapped phase time-series from the stack of SAR images. Phase linking methods are mainly non-linear observational functions including maximum likelihood (Ferretti et al., 2011; Guarnieri and Tebaldini, 2008; Spaans and Hooper, 2016) and eigenvalue decomposition estimators (Fornaro et al., 2015), which use all possible interferometric pairs, known as the full covariance/coherence matrix. To use the simplicity of linear observational functions, the integer least square (ILS) method (Samiei-Esfahany et al., 2016) was proposed which can be applied to the full covariance matrix or any subset of interferograms at more computational cost. Although phase linking methods provide more efficiency from an estimation point of view, one of the main drawbacks is that they are computationally expensive. This problem can be overcome using the sequential processing technique (Ansari et al., 2017, 2018).

Comparing PS and SBAS techniques, an inconsistency between the displacement velocity from the two techniques was observed (Lauknes et al., 2006; Shanker et al., 2011) but the source of inconsistency was not understood and was interpreted to be in the expected noise levels. More recently, Ansari et al. (2021) attributed the observed inconsistency to a systematic bias known as fading signal that presents in short temporal baseline interferograms and decays when using interferograms with larger temporal baselines. They suggest that implementing a full network of interferograms in non-linear phase linking techniques, would reduce the amount of bias in the final displacement time-series and estimated velocity. De Luca et al. (2022) consider the so-called bias as a noise which introduces a non-zero closure phase and can be filtered out. In this paper we address the contributions of both decorrelation and the systematic bias leading to non-zero closure phase and reducing the achievable precision of InSAR time-series. We provide a generalized approach that minimizes the amount of bias for all pixels.

The existing open-source InSAR time-series analysis softwares use the small baseline approach (Miami INsar Timeseries software in Python, Yunjun et al., 2019; GIAnT, Agram et al., 2013; LicsBAS, Morishita et al., 2020) or the persistent scatterer approach (StaMPS, Hooper et al., 2007; 2004). In this paper, we present a python package named MiaplPy (MIAMI Phase Linking software in PYthon) for non-linear time-series analysis using the full covariance matrix phase linking approach.

This paper is organized as follows. First, we briefly summarize the theoretical idea of PS and DS selection, each non-linear phase linking method and the sequential processing technique (section 2). We next assess the performance of the methods by applying them to simulated data (section 3). Then we compare unwrapping pair selection strategies (section 4) and describe the workflow implemented in our package (section 5). Finally, we show the application on real data compared with the small baseline approach (section 6) followed by a discussion (section 7).

2. Theoretical basis

2.1. Types of scatterers candidate for time-series analysis

The PS pixels are dominated by targets within the pixel showing a coherent phase time-series and distinguished from neighboring pixels with high signal-to-noise ratio. In contrast the DS pixels contain groups of moderate scatterers slowly decorrelate over time and they share the same behavior with their neighboring pixels. To increase the coherence magnitude over DS pixels, commonly the complex interferograms are multi-looked, i.e., they are averaged around a neighborhood of the pixel of interest. The multi-looking can be done over a predefined boxcar window with certain shape in range and azimuth directions or can be applied on a group of pixels identified as self-similar neighbors (referred to as Statistically Homogeneous Pixels (SHPs) in Ferretti et al. (2011)) as we further discuss in section 5.2.

The procedure of boxcar multi-looking (used in traditional interferometry and classic SBAS algorithm) can increase the coherence and signal to noise ratio for DS pixels but it will mix the scattering from neighboring pixels that may not be homogeneous and may not necessarily reflect the same physical processes. Nevertheless, boxcar or self-similar multi-looking can give rise to non-closing triplets or phase closure C_{njm} which is defined as

$$C_{njm} = \Delta\varphi_{nj} + \Delta\varphi_{jm} - \Delta\varphi_{nm} \quad (1)$$

where nj , jm and nm are wrapped interferometric phase between images acquired at time n , j and m . The non-closing triplets can arise from different sources such as temporal decorrelation, processing errors (e.g., inconsistent pairwise coregistration, pairwise flattening and pairwise geocoding), or physical processes that change the dielectric constant of the scattering targets between different acquisitions such as moisture change which lead to spatial and temporal inhomogeneity in the multi-looking neighborhood (Zheng et al., 2022). Depending on the source of the closure phase, they can lead to noisy estimation of the time-series (closure phases originating from decorrelation) or can add up during interferogram inversion and produce systematic bias (closure phases originating from processing errors or physical causes) (Zheng et al., 2022).

The non-zero closure phase caused by the spatial inhomogeneity of pixels in a multi-looking window can be reduced by multi-looking the self-similar neighbors in the window. However, temporal inhomogeneity cannot be eliminated or reduced by self-similar multi-looking. Regardless of the source of the closure phase, the impact of the closure phase on the InSAR displacement time-series is minimized by using all possible interferometric phases (Ansari et al., 2021) which can be best implemented in full covariance method algorithms. The impact of closure phase on classic SBAS time-series can be estimated from a sufficiently redundant network of triplets (Zheng et al., 2022).

We implement an InSAR time-series analysis method that uses all possible interferometric pairs multi-looked over self-similar neighbors. Multi-looking over self-similar neighbors reduces the impact of spatial inhomogeneity by treating different targets properly based on their scattering mechanism and preserves the native spacing of the SAR images during the displacement time-series estimation. To distinguish between different targets and scattering properties, we review the definition and properties of the interferometric covariance matrix associated with a target multitemporal observation vector. Assuming N properly coregistered SAR images, for a pixel at location x a complex $N \times 1$ target vector d is given by:

$$d_x(A, \theta) = \left[A_x^1 e^{i\theta_x^1}, A_x^2 e^{i\theta_x^2}, \dots, A_x^N e^{i\theta_x^N} \right]^T \quad (2)$$

where A_x^j , θ_x^j indicate amplitude and phase of pixel x at time j and T denotes transposition. Let's assume Ω to be a set of M self-similar neighboring pixels that are statistically homogeneous and contributing

to estimate the $N \times N$ covariance matrix C :

$$\hat{C}_{ij} = \frac{1}{M} \sum_{x \in \Omega} d_x^i d_x^{jH} \quad (3)$$

where H indicates the Hermitian conjugate operation.

The complex interferometric coherence matrix is obtained by normalization of the covariance matrix:

$$|\Gamma_{ij}| = |C_{ij}| / \sqrt{\sum_{x \in M} |A_x^i|^2 \sum_{x \in M} |A_x^j|^2} \quad (4)$$

Where Γ_{ij} and C_{ij} are the elements of the coherence matrix and covariance matrix respectively corresponding to images i and j , and $||$ indicates absolute value. As it was described by Ferretti et al. (2011), the absolute values of the coherence matrix are representative of the interferometric correlation ranging between 0 and 1 and the phase of the off-diagonal elements are the averaged phase of each interferogram. The coherence matrix of an ideal PS has all correlation values equal to 1. Therefore, it is singular with a zero determinant and has only one non-zero eigenvalue and a corresponding eigenvector showing the target behavior (De Zan and Rocca, 2005; Ferretti et al., 2011). With that in mind, PS and DS are different based on the number of pixels contributing to the estimation of the covariance matrix. Accordingly, using the self-similar neighbors helps to have a less biased estimation of the covariance matrix.

The set of self-similar neighbors include the pixel itself, so for an ideal PS, the number of self-similar neighbors equals to 1 but as the pixel shows more DS behavior, the number of them increases. Self-similar neighbors for each pixel are found by running a statistical test such as the Kolmogorov-Smirnov test (KS), on a window of neighboring pixels (Ferretti et al., 2011). Since the PS pixels are not ideal and they might share properties with neighboring pixels, such as pixels on the roof of a building, we first select PS and DS pixels using a threshold on the number of self-similar neighbors and then further remove the outliers. In our package PS pixels will be selected based on two criteria. The first criterion uses the eigenvalue statistical analysis method of Navneet et al. (2018) for PS selection, which is based on the percentage of contribution of the top eigenvalue of the coherence matrix. Therefore, among PS pixels, those pixels for which the top eigenvalue does not show a high percentage of contribution compared to other eigenvalues and follows Tracy-Wisdom distribution (Hoyle and Rattray, 2004), will be rejected as noisy pixels. The second criterion uses amplitude dispersion to select the PS pixels (Ferretti et al., 2001), which is the ratio of the standard deviation and mean of the amplitude of the SAR stack.

DS pixels, on the other hand, will be selected based on the temporal coherence after the non-linear phase linking. The temporal coherence is calculated using initial (θ_n) and estimated (φ_n) phase values of a pixel (Ferretti et al., 2011):

$$\gamma = \frac{1}{N^2 - N} \sum_{n=1}^N \sum_{m \neq n}^N e^{i\theta_{nm}} e^{-i(\varphi_n - \varphi_m)} \quad (5)$$

where N is the number of images. Temporal coherence is a measure of the goodness of fit for the estimated wrapped phase time-series.

2.2. Non-linear phase linking methods

The covariance matrix (as well as the coherence matrix) is a key statistic for retrieving phase time-series in phase linking approaches. The coherence matrix is preferred because it compensates for the imbalance between SAR image amplitudes (Cao et al., 2016). Due to the contribution of different decorrelation sources, the estimation of this matrix is always biased, and the solution of coherence matrix inversion is suboptimal. The best solution is the one having variance close to Cramér-Rao lower bound (CRLB) (A. Monti Guarneri and Tebaldini, 2008; 2007), which is the lower bound of the theoretical variance of the

unbiased estimators, i.e., CRLB is the most accurate that an unbiased estimator can get. The three algorithms in our package use the coherence matrix as an input for phase linking, therefore they analyze the full network of interferograms for each pixel's neighborhood. Following is a summary of each method.

2.2.1. Phase triangulation

Assuming that target multitemporal vector of observations follow a complex circular gaussian distribution, the estimated coherence matrix can be used to estimate the target vector for each pixel by phase triangulation algorithm (PTA) (Ferretti et al., 2011; Guarneri and Tebaldini, 2008; De Zan and Rocca, 2005). PTA, also known as SqueeSAR, estimates the wrapped phase time-series by maximizing the probability distribution function of the data using repetitive optimization algorithms.

$$\Theta = \arg \max_{\Theta} \left\{ \Theta^H (|\hat{\Gamma}|^{-1} \circ \hat{\Gamma}) \Theta \right\} \quad (6)$$

In this equation, Θ is the vector of $N - 1$ estimated phase values assuming the first image is zero, in other words, $N - 1$ single-reference interferograms, $\hat{\Gamma}$ is the estimated complex coherence matrix obtained from normalizing the covariance matrix, H indicates Hermitian conjugation and \circ denotes the Hadamard (entry-wise) product.

The PTA estimator theoretically provides the optimum solution as far as the unbiased coherence matrix is known. The convergence of this method depends on the initial values of the sought phase time-series, and it is computationally expensive.

2.2.2. Classic eigenvalue decomposition

The classic eigenvalue decomposition phase linking method of Fornaro et al. (2015), referred to by them as CAESAR and EVD by other studies (Ansari et al., 2017, 2018; Fornaro et al., 2015; Navneet et al., 2018; Samiei-Esfahany et al., 2016), finds the maximum eigenvalue of the covariance matrix assuming the corresponding eigenvector is representative for the dominant scattering mechanism. This approach is computationally efficient, but it is a suboptimal solution. We refer to this method as classic eigenvalue decomposition (CED) as there are other methods that use eigenvalue decomposition.

2.2.3. Eigenvalue decomposition-based maximum likelihood

The eigenvalue decomposition-based maximum likelihood of Interferometric phase method dubbed EMI by Ansari et al. (2018), in which a generalization is applied to the covariance model using Lagrange multipliers, was shown to have both estimation optimality and computational efficiency (Ansari et al., 2018). The estimation of phase time-series is via eigen decomposition:

$$(|\hat{\Gamma}|^{-1} \circ \hat{\Gamma}) \hat{\nu} = \lambda_m \hat{\nu} \quad (7)$$

The eigenvector ($\hat{\nu}$) corresponding to the minimum eigenvalue (λ_m) is the sought solution.

It worth noting that estimation of $|\hat{\Gamma}|^{-1}$ requires the matrix to be positive definite. If the condition is not met, a regularization is required by adding a damping factor to negative eigenvalues. The regularization is required for EMI and PTA where we need $|\hat{\Gamma}|$ to be invertible, hence a non-zero determinant is desired. If the regularization does not fix the problem for a pixel, the program would switch to the CED method. We call our strategy Combined eigenvalue maximum likelihood Phase Linking (CPL).

2.2.4. Short bandwidth

This approach is a modified version of the phase linking method that uses a partial coherence matrix, i.e., short temporal baseline interferograms and sets larger temporal baselines to zero. This method can be used to assess the estimated displacement time-series with different

numbers of consecutive interferograms. We refer to it as Short bandwidth (SBW). It is similar to the SB method except that it involves phase linking (Ansari et al. (2017) refer to this method as StBAS).

2.2.5. Sequential mode

The first three methods can be implemented in sequential mode (Ansari et al., 2017) which reduces computational costs. The idea of sequential estimator is to divide the full stack of N images into m ministacks, starting to process the first ministack, then compress it into one image via principal component analysis and then use the compressed image along with the images in the next ministack. If we assume the ν_m is the normalized phase linking solution of a ministack which is equivalent to the eigenvector corresponding to maximum eigenvalue in CED and Z is the ministack of single look complex images (SLCs), then the compressed SLC (\hat{Z}_c) is given by the following projection:

$$\hat{Z}_c = \nu_m^H Z \quad (8)$$

This procedure continues until all ministacks are processed, each with all the previous compressed images. The ministacks are connected after correcting the offsets through an additional phase linking between compressed images. The estimated phase values will be added to each ministack. This is referred to as datum connection by Ansari et al. (2017).

3. Performance analysis

We assess the performance of the non-linear phase linking methods with a simulation of the complex interferometric coherence matrix. The complex interferometric coherence $\Gamma_{m,n}$ between acquisitions m and n , is given by (Ansari et al., 2021; De Zan, 2020; De Zan & López-Dekker, 2011):

$$\Gamma_{m,n} = \left((\gamma^0 - \gamma^\infty) \exp \exp \left(-\frac{|\Delta t|}{\tau} \right) + \gamma^\infty \right) \exp \left(j\nu \frac{4\pi}{365\lambda} \right) \quad (9)$$

where t is the temporal baseline between the two acquisitions, λ the wavelength, γ^0 and γ^∞ the short-term decaying and long-term persistent coherence, τ the temporal decorrelation constant and ν is the ground velocity. The parameters are given in supplementary Table S1. For seasonal decorrelation, we substitute $(\gamma^0 - \gamma^\infty)$ in equation (9) with a sinusoidal component as $(A_S + B_S \cos(\frac{2\pi t_m}{180})) (A_S + B_S \cos(\frac{2\pi t_n}{180}))$ (eq. (30) of Even and Schulz, 2018) where t_m and t_n are the temporal baseline from the first acquisition. The values of A and B are calculated from $\gamma^0 = (A_S + B_S)^2$ and $\gamma^\infty = (A_S - B_S)^2$.

We simulate a dataset of 100 images with 6 days temporal baseline between acquisitions, a constant velocity of 4 mm/yr and four different temporal correlation scenarios: long-term coherent, long-term decorrelated, light seasonal decorrelation and strong seasonal decorrelation.

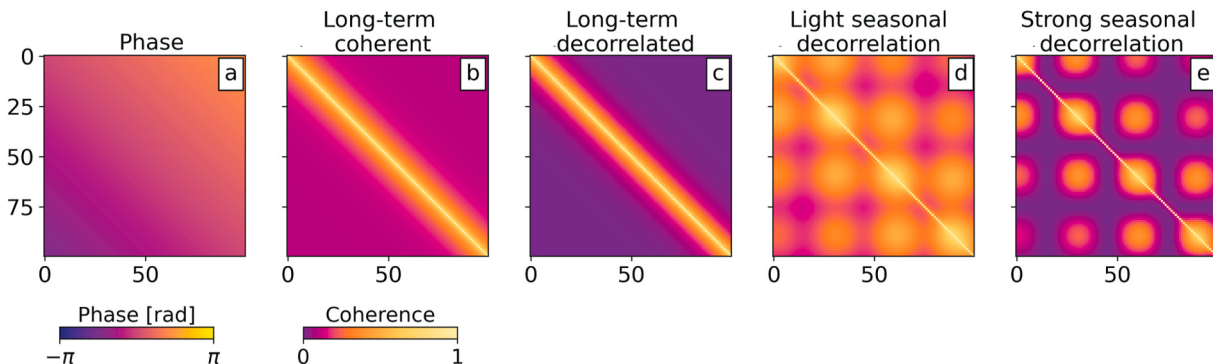


Fig. 1. Simulated complex coherence matrix for four different temporal correlation models. (a) Phase values of the matrix for a signal with constant velocity of 4 mm/yr. Absolute values of the matrix (correlations) for (b) the long-term coherent model, (c) long-term decorrelated model, (d) light seasonal decorrelation and (e) strong seasonal decorrelation models. The phase values are identical for all four models.

The phase values and the absolute values (correlations) of the simulated complex coherence matrices are shown in Fig. 1. The phase values of the matrix range from 0 to 1.46 rad (6.5 mm) (Fig. 1a) and are the same for all four models. The correlation values vary from 0 to 1. The temporal decorrelation constant is 50 days for the first two models. For seasonal decorrelation models, indicates the period including two coherent seasons where the correlation is high in the coherence matrix and is set to 400 days.

To investigate the performance of the phase linking approaches we generate 300 self-similar pixels by multiplying the noise free simulated coherence matrix with synthetic phase noise (a vector of random complex circular gaussian distributed numbers). We then estimate the coherence matrix using the generated 300 noisy self-similar neighbor vectors. The inherent averaging in the calculation of coherence matrix using the self-similar neighbors performs despeckling on the phase and amplitude of the target pixel.

The phase values of the complex coherence matrix (first column of Fig. 2) which are representing all possible interferograms despeckled for a pixel using 300 self-similar neighbors, show how they are altered according to the temporal coherence model (Table S1). Interferograms that have longer temporal baselines show rapid phase changes and complete decorrelation for long-term decorrelated (Fig. 2c and d) and strong seasonal decorrelation models (Fig. 2g and h), but slowly decorrelate for long-term coherent (Fig. 2a and b) and light seasonal decorrelation models (Fig. 2e and f).

We invert for the wrapped phase time-series from the estimated coherence matrix using different phase-linking methods (CED, PTA and EMI) with and without sequential mode. For the sequential mode, we divide the whole stack of images into ministacks with a size of 10 SLCs. To assess the estimated phase values, we perform 1000 realizations and calculate the root mean square error (RMSE) of the differences between estimated and the original simulated phase time-series:

$$RMSE = \sqrt{\sum_{i=1}^N (\theta_i^{est} - \theta_i^{sim})^2 / (N-1)} \quad (10)$$

where N is the number of images, θ_i^{est} is the i^{th} element of estimated phase vector and θ_i^{sim} is the i^{th} element of noise-free simulated phase vector. We also perform the short bandwidth method using a bandwidth of 4 successive images to compare with full coherence matrix implementation.

3.1. Simulation results

Fig. 2i-l shows the RMSE for the long-term coherent scenario (Fig. 2i), the long-term decorrelated scenario (Fig. 2j) and the same but with light and strong seasonal decorrelation (Fig. 2k, l, respectively).

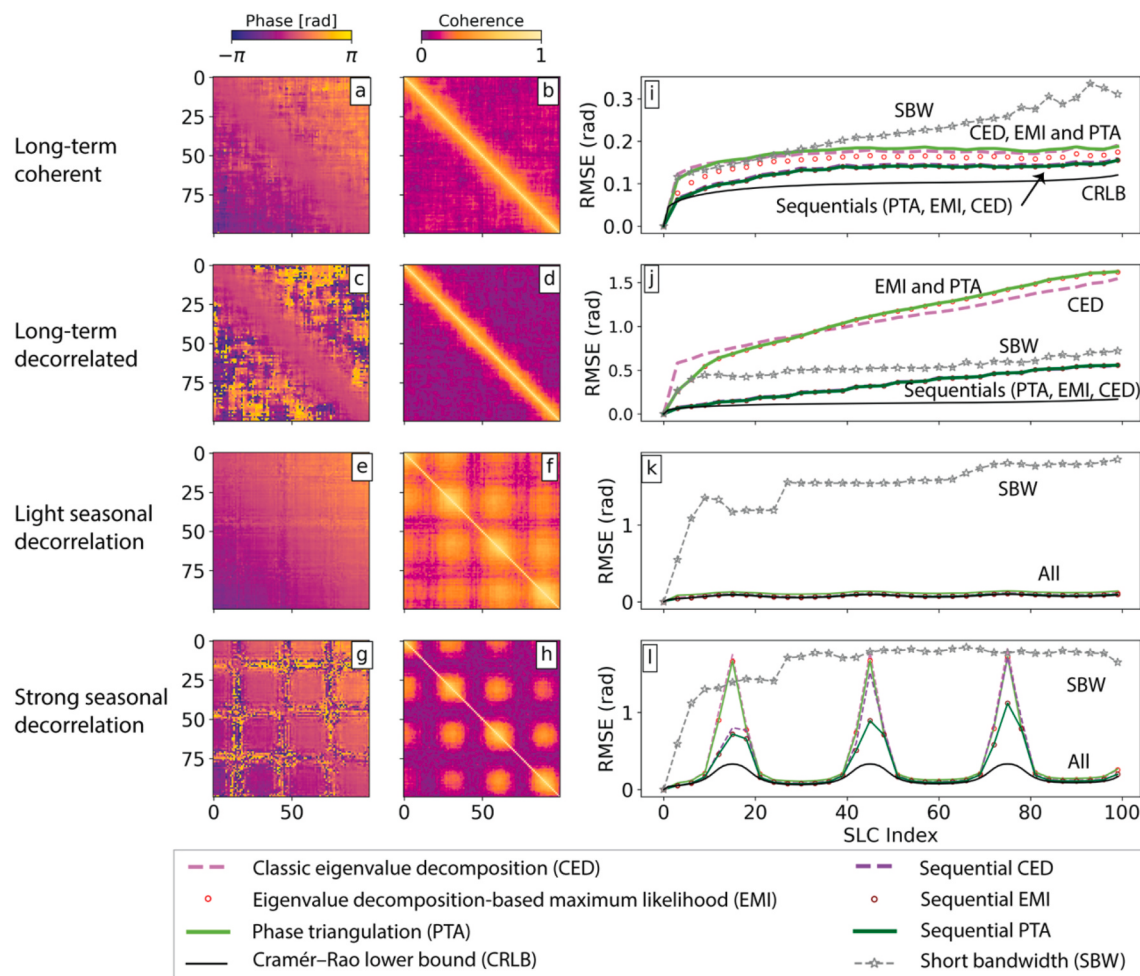


Fig. 2. Assessment of different phase linking methods relative to Cramér–Rao lower bound (CRLB) using simulated data with noise. Phase and absolute values of estimated coherence matrix and RMSE of the phase linking results for (a, b, i) the long-term coherent scenario, (c, d, j) the long-term decorrelated scenario, (e, f, k) the light seasonal decorrelation scenario, and (g, h, l) the strong seasonal decorrelation scenario.

Comparing the RMSE values with Cramér–Rao lower bound (black solid line) indicates the performance close to optimum for all methods when the model is coherent or has light seasonal decorrelation (Fig. 2i, k). The challenge is for long-term decorrelated (Fig. 2j) and strong seasonal decorrelation (Fig. 2l) models. We can see that the RMSE increases gradually from beginning to the end of the stack for the long-term decorrelated scenario. Classic eigenvalue decomposition turns out to have a slightly better performance compared to phase triangulation and eigenvalue decomposition-based maximum likelihood in non-sequential mode when there are more than 40 images in the dataset. However, the RMSE values obtained from sequential methods are significantly smaller.

For the strong seasonal decorrelation model, we observe large RMSE values only for the times we have lost correlation and values close to optimum for the coherent times. The main difference between sequential mode and non-sequential mode comes from the decorrelation model. For long-term decorrelated model, sequential mode improves RMSE by 0.75 ± 0.2 rad which is significant and without sequential mode, a potential DS will be masked out as noise. The improvement of average RMSE is smaller for strong seasonal decorrelation model and it is in the range of 0.08 ± 0.2 rad, however the maximum RMSE for strong seasonal decorrelated model reaches to $2\pi/\sqrt{12}$ rad which is the standard deviation of uniform distribution of the wrapped phase, i.e. the estimated wrapped phase in simulated winter with complete correlation loss is just noise randomly sampled between $-\pi$ and π (Fig. 2l).

The RMSE result of short bandwidth is also shown for each scenario.

Comparing the RMSE obtained, we see that short bandwidth is only performing better than full coherence matrix estimation in the case that there is a long-term decorrelated model which is exponentially decorrelating with time, however the sequential mode still has an amount of $0.19 - 0.42$ rad lower RMSE.

Focusing on strong seasonal decorrelation simulations, we see the potential of non-linear phase linking methods for information retrieval. In reality, the seasonal behavior is very common in cultivated lands and regions with snow fall. As expected, the short temporal baseline methods like classic SBAS do not perform well in such conditions. In practice, classic SBAS analysis in such regions usually requires removing images that are acquired in winter seasons because of high decorrelation. Removing interferograms in classic SBAS can lead to a disconnected network of interferograms or low temporal coherence that reduces the number of selected DS pixels. Our observations from simulated data, shows that even in the presence of seasonally complete correlation loss, we can still process all the images using the full coherence matrix, such that we obtain more accurate estimations at coherent acquisitions and noisy estimates at acquisitions with complete correlation loss.

4. Unwrapping error propagation

The wrapped phase time-series, resulting from different phase linking methods, should be unwrapped using 2D (e.g., Chen and Zebker, 2002) or 3D (e.g., Costantini et al., 2002) phase-unwrapping algorithms to obtain the unwrapped phase time-series from which the range change

(displacement) time-series can be inferred. Here we discuss a network-based 2D phase-unwrapping approach which requires the selection of a network of image pairs for interferogram formation, unwrap each pair and invert the unwrapped interferograms to estimate the unwrapped phase time-series. Hereafter, we refer to the interferogram unwrapping networks as unwrapping networks.

Unwrapping a single-reference network directly gives the unwrapped phase time-series because the system is determined, i.e., the number of unknowns equal to the number of observations. Other possible unwrapping networks include a Delaunay network, connected annual single-reference interferograms (annual ministacks), and sequential networks with various numbers of consecutive image pairs without or with the inclusion of long-term (e.g., annual) interferograms. These networks are overdetermined (redundant) and unwrapped interferograms are solved for the unwrapped phase time-series using the generalized inverse of the design matrix which can propagate phase-unwrapping errors to the displacement time-series.

4.1. Simulated data

To assess how the phase-unwrapping errors are propagated, we simulate a zero-displacement time-series and generate six different networks of interferograms with three phase-unwrapping error distributions. In the three distribution cases the interferograms have 10 percent random unwrap errors (-2π or 2π), 30 percent random unwrap errors, and seasonal unwrap errors during a three-month period. The random distributions are meant to be a simplified representation of long-term coherent (10 percent) and long-term decorrelated (30 percent) coherence models in section 3 with unwrap errors of the same magnitude. The six networks are the single-reference network, the Delaunay network, an annual mini-stack network, and sequential networks with 1, 3 and 8 connections (see Figure S2.1 in the supplemental information; we use the baselines of 58 Miami Sentinel-1 images). We use both the L1- and L2-norms to solve the system. The L1-norm is more robust than the L2-norm for large numbers of outliers (unwrap errors). Lauknes et al.

(2011) used an L1-norm minimization using iteratively reweighted least squares. Wang et al. (2019) added a smoothing constraint.

We assume C-band frequency to convert unwrapped phase to range-change and use a smoothing constraint of 0.001 for the L1-norm solution. Fig. 3a shows the simulation result for a single-reference network where the estimated time-series at each acquisition relative to the reference acquisition is unwrapped independently of other acquisitions and therefore phase-unwrapping errors don't propagate. For this reason, for all three unwrap error distributions the estimated time-series is offset from zero by half of the radar wavelength, equivalent to 2π unwrapping error at the corresponding acquisitions. The sequential network with one connection, is also determined with one unique solution for both L1- and L2-norm minimizations, however in the timeseries, every acquisition depends on the previous ones, therefore all unwrapping errors propagate and accumulate toward the end of the timeseries. The other networks are redundant, and the generalized inverse propagates the unwrapping errors into multiple dates. A non-zero displacement time-series with tropospheric delays shows to propagate the errors similarly (Supplementary Figure S2.2).

To quantify the performance of the different networks we run 1000 realizations and for each we compute the RMSE of the estimated time-series (Supplementary Figure S2.3; Table S2.1). For the 10% unwrap error distribution and with L2-norm minimization for the network inversion, the Delaunay network (median and median absolute deviation of the RMSE of $0.58 \pm 0.10 \text{ cm}$) performs better than the annual ministack network ($0.91 \pm 0.04 \text{ cm}$) and the sequential network with 1 connection network ($2.60 \pm 0.63 \text{ cm}$) (Fig. 3a). We find similar results for the 30% unwrap error and the seasonal unwrap error distributions (Fig. 3b and c).

Additional connections improve the performance of the sequential network (0.76 ± 0.18 and 0.33 ± 0.07 for 3 and 8 connections in the 10% unwrap error distribution, respectively) by spreading the unwrap error to more connections with lower magnitudes. This improvement comes with an increase in the number of interferograms to unwrap by a ratio of 1.7 and 2.7 compared to the Delaunay network which results in a

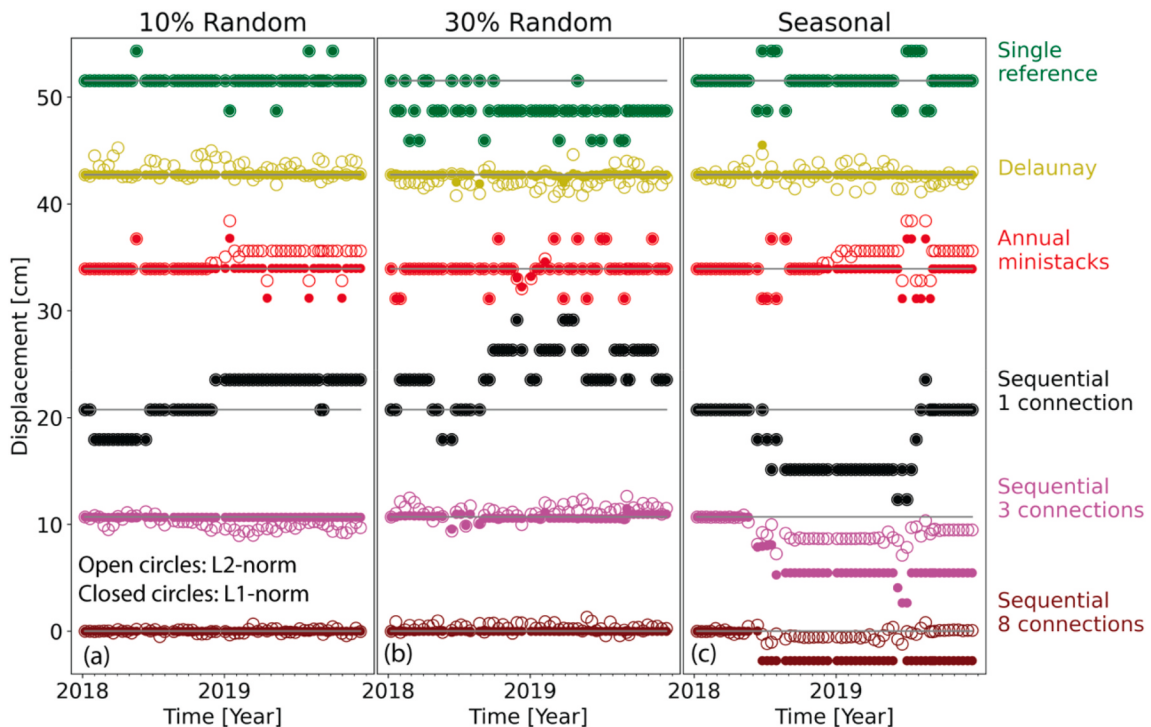


Fig. 3. Simulated unwrap error propagation for (a) 10% random unwrap errors, (b) 30% random unwrap errors, (c) seasonal unwrap errors (during 3 months period) for different unwrapping networks using L1 and L2 norm minimization. Solid line is the simulated zero velocity time-series. single-reference and the sequential network with 1 connection are determined systems and have unique solution for L1-and L2-norm minimizations.

double to triple computational time.

Comparing L1-and L2-norm minimization, the 10% and 30% random unwrap error distributions show better performance of the L1-norm for all networks. For the seasonal unwrap error distribution, we observe the best performance with the Delaunay network using the L1-norm. The drawback of the L1-norm is that it is a computationally very expensive iterative approach.

Fitting a linear velocity model to the time-series obtained from above experiment, we observe the unimodal distribution of the velocities to be consistent with the RMSE and conclude that Delaunay network provides an accurate and precise estimation compared to other networks, hence it is the optimum network in our analysis (Supplementary Figure S2.4; Table S2.2).

In conclusion, for time-series of a few years we suggest using a single-reference network, because (i) the unwrap error does not propagate to all acquisitions in the time-series, (ii) their non-propagated unwrap error in individual interferograms (i.e., acquisition dates compared to the reference acquisitions) facilitate unwrap error detection in the time-series by post-processing algorithms, and (iii) is the fastest network to unwrap as its total number of interferograms are one third of Delaunay and one fifth of sequential with 5 connections. In specific circumstances of strong seasonal decorrelation or generally large and frequent unwrap errors caused by long-term decorrelation, we suggest using L1-norm minimization of Delaunay network for more accuracy, with the cost of extra computations.

4.2. Real data

To evaluate the impact of unwrapping networks on error propagation we also consider real wrapped phase time-series data obtained by

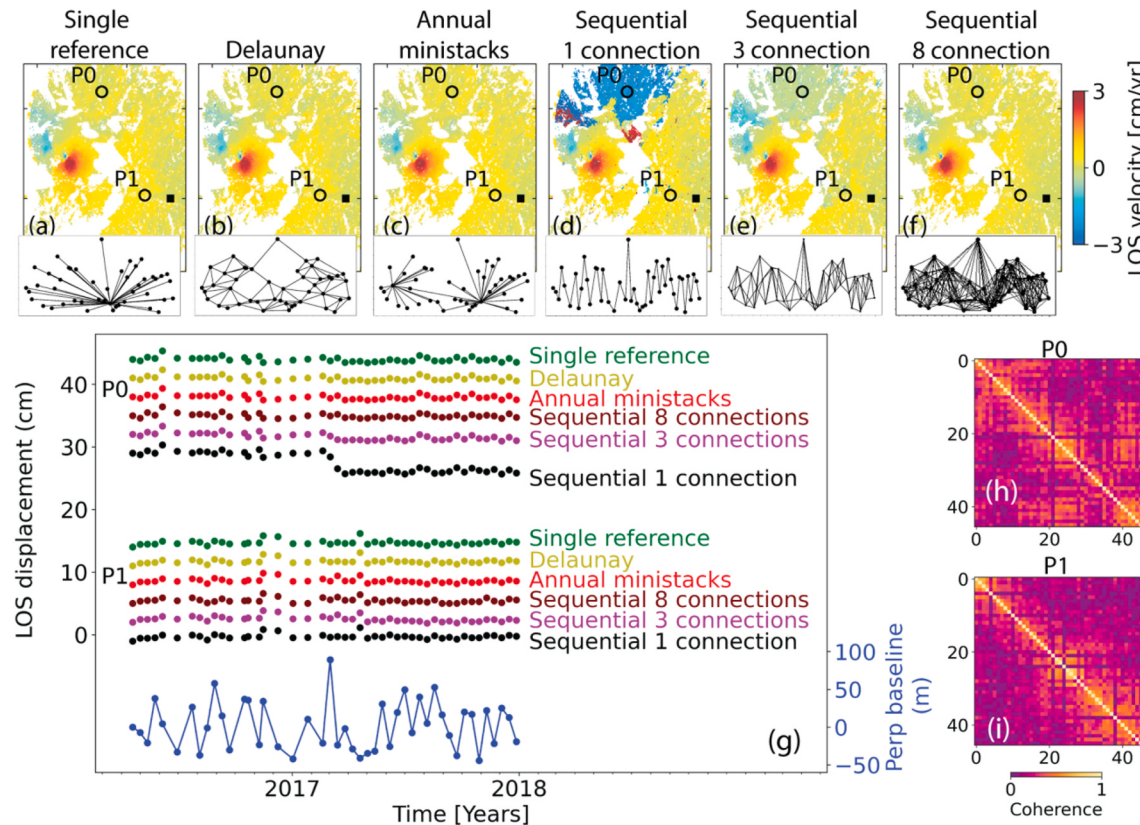


Fig. 4. Unwrapping strategy assessment. Velocity maps for the same networks in section 4.1: (a) single-reference network, (b) Delaunay network, (c) annual ministacks network, (d) sequential network with 1 connection, (e) sequential network with 3 connections and (f) sequential network with 8 connections. The unwrapping networks are shown on each panel. (g) Displacement time-series for points P0 and P1 for unwrapping of different networks. Lower part of (f): perpendicular baseline. (g, h) Coherence matrices for points P0 and P1.

the combined phase linking approach over Guagua Pichincha volcano in Ecuador and Mount Lassen volcano in California (described later in the paper in section 6). The processing workflow is described in section 5. For each site the same wrapped phases are unwrapped using several types of unwrapping networks. Since we form the networks of wrapped interferograms from a wrapped phase time-series, the closure phases of all possible triplets in the network are zero. Differences in the obtained displacement time-series and velocities are entirely due to the propagation of the unwrap errors from individual interferograms to the estimated displacement at each time-series epoch. Unwrapping of the Guagua Pichincha phase time-series leads to randomly distributed unwrap errors, whereas unwrapping the phase time-series of the seasonally snow-covered Mount Lassen leads to seasonal unwrap error distribution.

4.2.1. Guagua Pichincha volcano

In Fig. 4 we compare the velocity and displacement time-series obtained using different unwrapping networks for a sample dataset of 46 images over Guagua Pichincha volcano. We consider the same unwrapping networks as in section 4.1 (Fig. 4a-f). Any differences between the velocity maps are caused by phase-unwrapping errors. They occur at incoherent pixels separating coherent regions causing discontinuities between them which then propagate into the estimated time-series and velocity. Decorrelated areas with phase-unwrap errors have been masked out. The differences are quantified with RMSE of the difference between each network and the single-reference network and show the highest RMSE (1.11 cm/yr) for the Sequential network with 1 connection, while for Delaunay, annual ministacks and sequential network with 8 connections, the RMSE is at the same level ($\sim 0.15 - 0.19 \text{ cm/yr}$) (Table S2.3 and Figure S2.5).

Discontinuities between coherent regions are most evident for the

non-redundant sequential network with 1 connection (Fig. 4e), where a blue region in the upper part is offset from the rest of the velocity map by $\sim 3 \text{ cm/yr}$. For the redundant sequential networks with 3 and 8 connections the same region is offset by smaller amounts ($\sim 0.5 \text{ cm/yr}$ and $\sim 0.05 \text{ cm/yr}$) (Fig. 4d) because the unwrap error is distributed to more dates as shown in Fig. 3. Such discontinuities are absent in the velocity maps obtained with the single-reference, Delaunay and annual ministack networks.

The estimated time-series for point P0 shows a jump of $\sim 3 \text{ cm}$ around March 2017 for the sequential network with 1 connection (non-redundant) and a jump with smaller magnitude for the sequential network with 3 connections (redundant). P0 is located in a region disconnected by steep topography which most likely has caused unwrapping errors in the interferograms including the March 2017 acquisition (spatial baseline of up to $\sim 80 \text{ m}$). The time-series at P1 is consistent among all different networks most likely because it is located in the same coherent region as the reference pixel.

These spatial and temporal discontinuities show that in this case (i) the sequential unwrapping networks are most affected by phase-unwrapping errors, and (ii) the impact of phase-unwrapping error decreases with increasing number of connections (pairs) in the network, consistent with the observations from the simulated data.

4.2.2. Mount Lassen volcano

We compare the same networks as the previous case except for the sequential networks with 1 and 8 connections. Also, we examine 5 years of data to better capture the impacts of seasonality. The velocity maps obtained from the single-reference and Delaunay unwrapping networks are similar (Fig. 5a and b) but not those from the annual ministacks and the sequential 3 connections network. The RMSE of the velocity differences between the Delaunay, the annual ministacks and the sequential network with 3 connections with respect to the single-reference network, are 0.19, 0.46 and 1.37 cm/yr , respectively (Table S2.3 and

Figure S2.6). These differences arise because the unwrapping errors during winter season propagate to subsequent acquisition dates as expected based on the simulations.

For this case study, the outcome of unwrapping error propagation for the annual ministacks network is a negative LOS velocity (apparent subsidence) which can be observed at points P1 and P2 in Fig. 5c (blue colors) and a decrease in LOS displacement (Fig. 5e). Similarly, for the sequential network, the outcome is a positive LOS velocity (apparent uplift), which can be observed at points P0, P1 and P2 in Fig. 5d (red colors) and an increase in LOS displacement (Fig. 5e).

The inconsistencies in time-series obtained from different unwrapping networks confirms that unwrapping error propagation depends on the design of the network. Another example for unwrapping error propagation for an agricultural area is shown in the [supplementary section S2E](#).

5. Workflow of non-linear phase linking processing

The input data for MiaplPy are coregistered SLCs. The workflow (Fig. 6) starts with phase linking of the wrapped phase time-series followed by phase-unwrapping and then inversion of the network of unwrapped interferograms. The MintPy software (Yunjun et al., 2019) is used for phase-unwrapping error correction (optional) and for the correction of the deterministic phase components of the time-series due to residual topography, tropospheric and ionospheric delay. In the following we describe the phase linking and phase correction steps.

5.1. Read a subset area of dataset

The starting point is reading the coregistered SLCs and geometry files including but not limited to latitude, longitude, height, incidence angle, heading angle and slant range distance. We recommend selecting a subset area to reduce the computational burden.

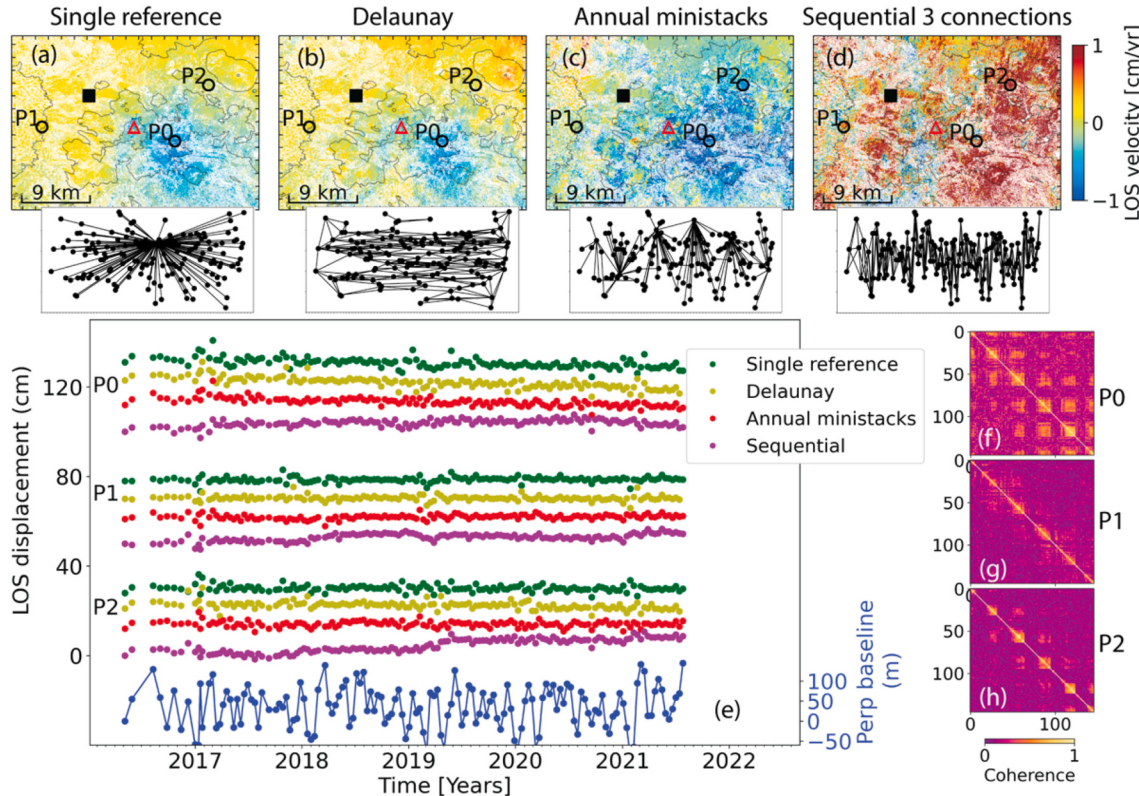


Fig. 5. Same as Fig. 4 except the sequential network with 1 and 8 connections but for Mount Lassen and with time-series for 3 points. For this case seasonal decorrelation applies.

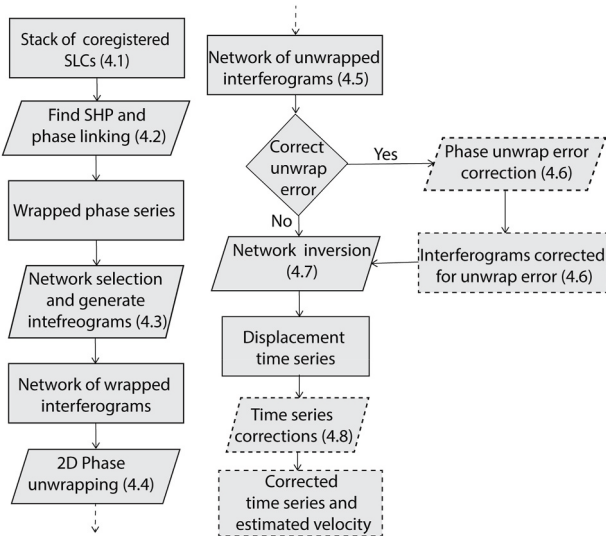


Fig. 6. Flowchart of non-linear phase linking and time-series analysis steps. Parallelograms: MiaplPy processing steps. Rectangles: input and output. Dashed boundaries: optional steps to be conducted by the MintPy software.

5.2. Finding self-similar neighbors and phase linking

For each pixel, a set of self-similar pixels will be selected within a given window. The default window size is 15 by 15 pixels in range and azimuth directions, respectively. Three statistical tests are available in MiaplPy for determining the self-similar neighbors, the two-sample Kolmogorov-Smirnov test (Stephens, 1970) which is the default, Anderson-darling (Scholz and Stephens, 1987) and t-test (Derrick et al., 2017; Shamshiri et al., 2018). The coherence matrix is estimated using the self-similar neighbors and then inverted using one of the phase linking methods described in section 2.2. PS candidates are identified as pixels with 10 or less self-similar neighbors and then further down-selected by two criteria of amplitude dispersion index (Fig. 7b) and top eigenvalue contribution percentage (Fig. 7c) described in section 2.1. The default threshold for the amplitude dispersion index is 0.42 and the threshold for the top eigenvalue contribution is 95%. Those pixels that satisfy both criteria are labeled as PS pixels, their SLC phase in the stack is extracted with respect to the first acquisition and stored as their wrapped phase series and their temporal coherence is set to 1. Applying the above-mentioned criteria, the final set of PS selected for a low-density urban area and golf club area is shown in Fig. 7e. For DS pixels the temporal coherence is estimated using equation (5) as a quality factor. The outputs are the linked wrapped phase time-series,

estimated temporal coherence, PS pixel mask and number of self-similar neighbors for each pixel.

Using sequential mode, two temporal coherence products are estimated, one with the full linked phase series after ministacks offset correction (Ansari et al., 2017) and one as an average of temporal coherence estimated for each ministack. The full version has lower values for pixels with strong decorrelation which masks majority of seasonally decorrelating pixels as well; however, pixels with seasonal decorrelation are reliable in coherent seasons, therefore, we prefer to use average temporal coherence to prevent masking of those pixels with seasonal decorrelation behavior. Fig. 8 shows the phase linking temporal coherence (labeled full temporal coherence in the software) and averaged ministack temporal coherence estimated for the sample dataset over Guagua Pichincha in Ecuador.

A pre-generated mask in radar coordinates can be given to accelerate the coherence matrix inversion at this step. Furthermore, the area is divided into small patches (default is 200 by 200) to resolve memory limitations and parallel processing is supported. After the phase linking, all patches are concatenated.

5.3. Unwrap network selection and interferogram generation

After the phase linking, we need to phase-unwrap a network of interferograms to obtain displacement time-series and the unwrapping is not error free. MiaplPy provides different image pair selection strategies to gain the best performance: sequential, annual ministacks, Delaunay

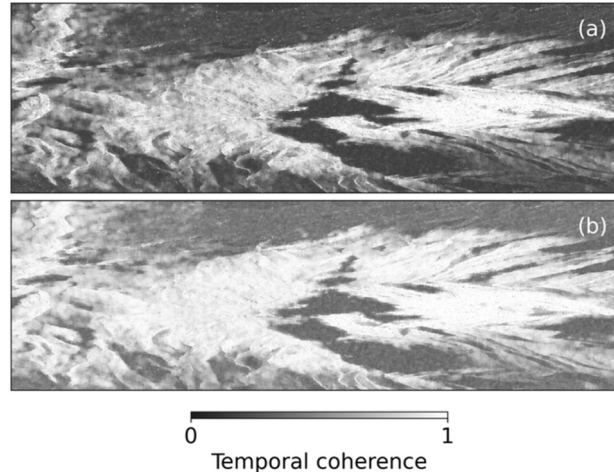


Fig. 8. (a) Full and (b) average temporal coherence (equation (5)) of inverted pixels for Guagua Pichincha.

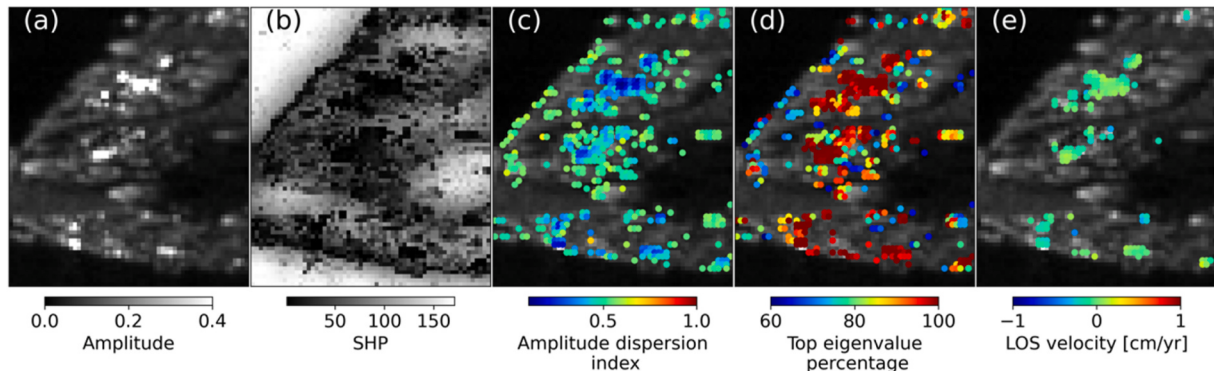


Fig. 7. PS selection parameters. (a) Average amplitude. (b) The number of self-similar neighbors for each pixel. (c) Amplitude dispersion index and (d) top eigenvalue contribution percentage of pixels with 10 or less number of self-similar neighbors respectively. (e) The final velocity map of the selected PS pixel for Indian Creek, Florida.

and single-reference pairs with or without adding annual interferograms. An assessment of the different strategies is presented in section 4.

5.4. Phase-unwrap interferograms

In this step the interferograms are phase-unwrapped using the two-dimensional phase-unwrapping algorithm of SNAPHU (Chen & Zebker, 2000, 2001, 2002).

5.5. Load unwrapped interferograms

In this step the phase-unwrapped interferograms from the previous step in full resolution are loaded to an HDF5 format adapted to MintPy to invert the network of unwrapped interferograms and perform different corrections supported by MintPy.

5.6. Interferograms correction

This step is done using MintPy modules and includes unwrapping network modification, reference point selection and unwrap error correction (Yunjun et al., 2019).

5.7. Network inversion

We need to convert the interferogram stack into displacement time-series. For this purpose, we use least square inversion of the unwrapped interferograms and convert the estimated unwrapped time-series to range-change time-series. Masking of the pixels is based on both temporal coherence from MiaplPy after the phase linking of the full coherence matrix and the temporal coherence calculated after the inversion of the unwrapped network of interferograms. The former represents the quality of the estimated wrapped phase time-series, and the latter represents the quality of the phase-unwrapping. The temporal coherence of unwrapped interferogram inversion is not meaningful for networks without redundancy such as the single-reference and annual ministacks networks. Users can also define other arbitrary masks.

5.8. Time-series corrections

Now that we have our displacement time-series, we can use MintPy for deterministic phase corrections such as topographic, tropospheric, and ionospheric correction.

5.9. Geolocation correction

The correct locations of the targets are important for urban infrastructure monitoring and geolocation correction is usually required especially for vertical infrastructures such as bridges and buildings. The height information from digital elevation models can't be used to precisely geolocate a target because they are either the elevation of the ground surface or top of the building if a digital surface model (DSM) is used. In either case, the scatterers detected in a SAR image come from different parts of the building from top to bottom. Therefore, the digital elevation models do not have the correct height for all the scatterers. We use the DEM error estimated in the topographic residual correction step of MintPy to correct for the geolocation offset (Jung et al., 2019). According to Fattah and Amelung. (2013) the topographic phase residuals are:

$$\varphi_{topo}(t_i) = \frac{4\pi}{\lambda} \frac{B_{\perp}(t_i)}{r \sin \sin(\eta)} \Delta H \quad (11)$$

where t is time, $B_{\perp}(t_i)$ is the perpendicular baseline between acquisition i and the reference, r is the slant range and η is the incidence angle. ΔH is the DEM error which we need for geolocation correction. Having the ΔH , we can calculate the relocation vector components in east-west and

north-south direction using the following equation (Jung et al., 2019) where α is the heading angle.

$$\Delta x = \Delta H \cot(\eta) \cos(\alpha) \quad \text{and} \quad \Delta y = \Delta H \cot(\eta) \sin(\alpha) \quad (12)$$

6. Application examples

We demonstrate the implemented phase linking approach using data for three volcanoes with different temporal coherence behavior, for Guagua Pichincha in Ecuador (section 6.2), Mount Lassen in Northern California (section 6.3) and the Three Sisters volcanic area in Oregon (section 6.4). In addition, we present data for the 2017 Mud Creek landslide, California, to demonstrate the high spatial resolution provided by the combined phase linking approach (section 6.5), the island of Miami Beach, Florida, to demonstrate the capability of PS measurements (section 6.6), and the Bristol dry lake in California to investigate the systematic bias (section 7.1). The test sites are shown in Fig. 9 and the data used listed in supplementary Table S2.

Guagua Pichincha is a high-risk volcano because the summit is located only 8 km west of Ecuador's capital city of Quito. The volcano has a horseshoe-shaped caldera open to the west with episodes of inflation and deflation (Morales Rivera et al., 2016). It erupted last in 2002. Mount Lassen is the southernmost Cascade volcano and erupted last in 1917. The Three Sisters volcanoes last erupted 2000 years ago but episodes of uplift have been detected since 2000 near south sister for an area of 20 kms in diameter (Lisowski et al., 2021). The Mud Creek landslide was triggered by a record rainfall after a long period of drought (Handwerger et al., 2019; Moretto et al., 2021) and buried the highway with 5 million cubic meters of debris. In the Miami area there is high interest in InSAR monitoring of coastal infrastructure following the tragic 2021 collapse of a coastal condominium near Miami Beach (Parkinson, 2021).

Sentinel-1 images were used for all applications because it is the only widely and freely available dataset, however the algorithm works for other data in different frequencies. An example of TerraSAR-X data is shown in the supplementary (Figure S3.12) for comparison.

We use the stack Sentinel package (Fattah et al., 2017) of the ISCE2 software for coregistering the SLCs. A few SLCs from before May 2016 were excluded because they have an incompatible Instrument Processing Facility (IPF) version (Piantanida et al., 2017). We use the SRTM DEM with ~30 m resolution (Farr et al., 2007) to remove the topographic phase component.

We use a window size of 19×9 (range \times azimuth) to find self-similar neighbors for each pixel. PS and DS pixels are selected based on criteria mentioned in section 2.1 and 5.2. For DS pixels we use the combined phase linking method to estimate the wrapped phase time-series.

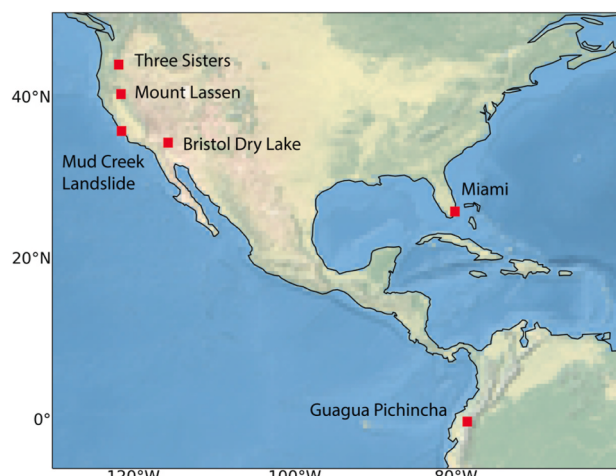


Fig. 9. Location map of study areas.

From the estimated wrapped phase time-series we generate different unwrapping networks of interferograms and unwrap each interferogram using SNAPHU (Chen and Zebker, 2000, 2001, 2002). We invert the network of unwrapped interferograms to estimate the unwrapped time-series and then convert to range-change time-series. We correct the estimated range-change time-series for tropospheric phase delay using ERA-5 data and Global Atmospheric Models (Hoffmann et al., 2019; Jolivet et al., 2011, 2014) and we correct for topographic residuals with a 2nd order polynomial temporal model (Fattah and Amelung, 2013) using MintPy. We use a temporal coherence threshold of 0.5 to mask out low-quality DS pixels.

For all cases we use a determined single-reference unwrapping network, except for Three Sisters for which we use the Delaunay network and L1-norm minimization. GNSS displacements are obtained from the Nevada Geodetic Laboratory (Blewitt et al., 2018) and projected into radar line-of-sight direction (LOS) using the image acquisition geometry.

6.1. Guagua Pichincha volcano

Guagua Pichincha is a sparsely vegetated volcano except for dense forests along the lower western flank. We compare the estimated displacement from combined phase linking with those from the classic small baseline technique (obtained using a sequential network with 4 connections, temporal coherence threshold of 0.8), and with GNSS data of station GGPA located on the uppermost eastern flank of the volcano. We reference both InSAR and GNSS to the QUI4 GNSS station in Quito.

The velocity map from the combined phase linking (Fig. 10a) has much better spatial coverage than the small baseline (Fig. 10b). It shows largely zero LOS velocity (green colors) in contrast to up to 1 cm/yr LOS velocity obtained from the small baseline (blue colors). The coherence matrices show that the temporal coherence behavior of pixels at GGPA in the nearly unvegetated summit area (Fig. 10d) is described by the

long-term coherent temporal coherence model, whereas pixel P0 (moss and grass land) is described by the long-term decorrelated temporal coherence model (Fig. 10e). In the time-series from the classic small baseline approach, a velocity difference of 2 mm/yr is observed for station GGPA and 10 mm/yr for point P0 (Fig. 10c) which are most likely introduced by unwrapping errors in the interferograms as they show large integer non-zero closure phase (Supplementary Figure S3.1). This example shows that phase linking can retrieve the signal for temporal coherence behavior described by the long-term decorrelated model.

6.2. Mount Lassen volcano

The summit area of this volcano is largely unvegetated, but the challenge is high seasonal decorrelation due to several months of snowfall. Therefore, even short temporal baseline interferograms lose coherence. The LOS velocity map from combined phase linking has a much better spatial coverage than from the small baselines approach (Fig. 11a and b). The latter has been obtained using a sequential network with 5 connections, complemented by one-year interferograms. Low coherent winter interferograms are removed (supplementary Figure S3.2). We use a temporal coherence threshold of 0.7. The displacement field obtained from phase linking shows a LOS velocity of $\sim -1 \text{ cm/yr}$ on the southeastern flank of the volcano in an area where there are no valid pixels from the small baseline approach. It is worth noting that linked phases have advantages for phase-unwrapping because phase linking filters for the temporal decorrelation and performs despeckling. Therefore, linked phases lead to better quality interferograms with higher spatial coherence than the original phases.

The coherence matrices show that station P665 exhibits a long-term decorrelated behavior (Fig. 11e) whereas P664 and P667 exhibit light and strong seasonal decorrelation, respectively (Fig. 11d, f). During the winter season the GNSS signal is lost because of snow coverage. InSAR data are still available and show less scatter than GNSS because the

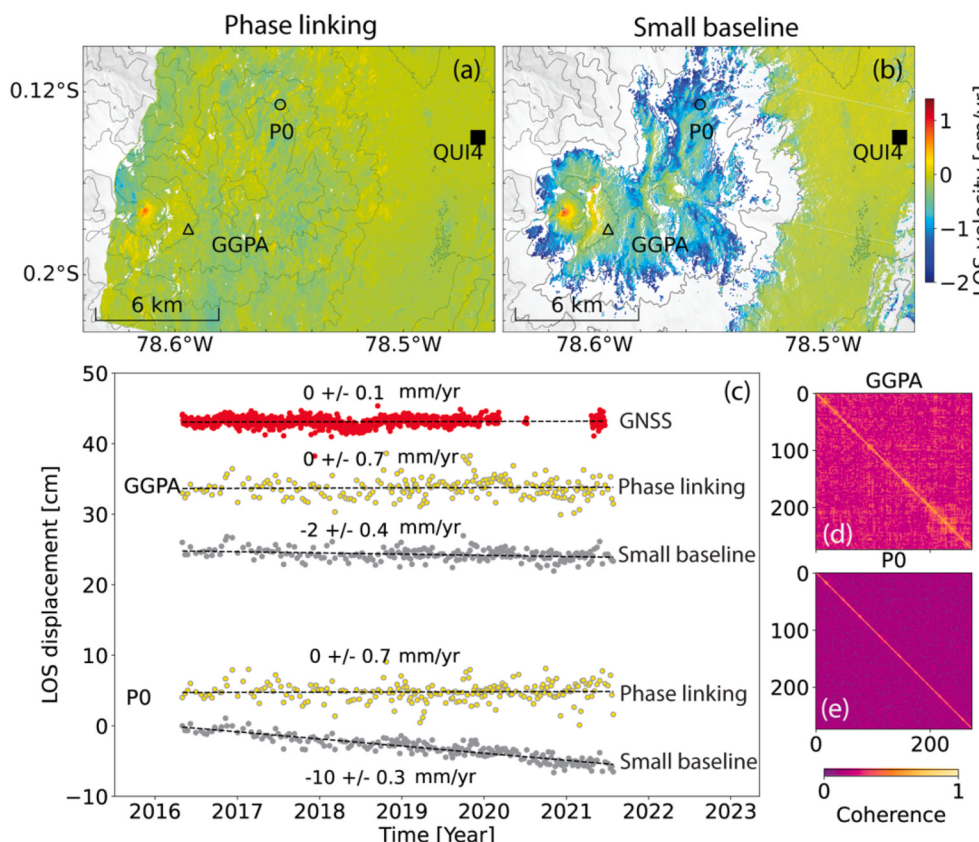


Fig. 10. LOS velocity from (a) phase linking with single-reference network for unwrapping, and (b) multi-looked small baseline approach using 4 sequential interferograms. QUI4 is the reference point. (c) Time-series for points GGPA and P0. (d, e) Coherence matrix for the GGPA and P0. Yellow, gray circles in c: phase linking, small baseline approach. In this and in the following figures phase linking results are shown as scatter plots with symbols larger than the pixel size, implying that data gaps appear smaller than they are in reality. (For interpretation of the references to color in this figure legend, the reader is referred to the Web version of this article.)

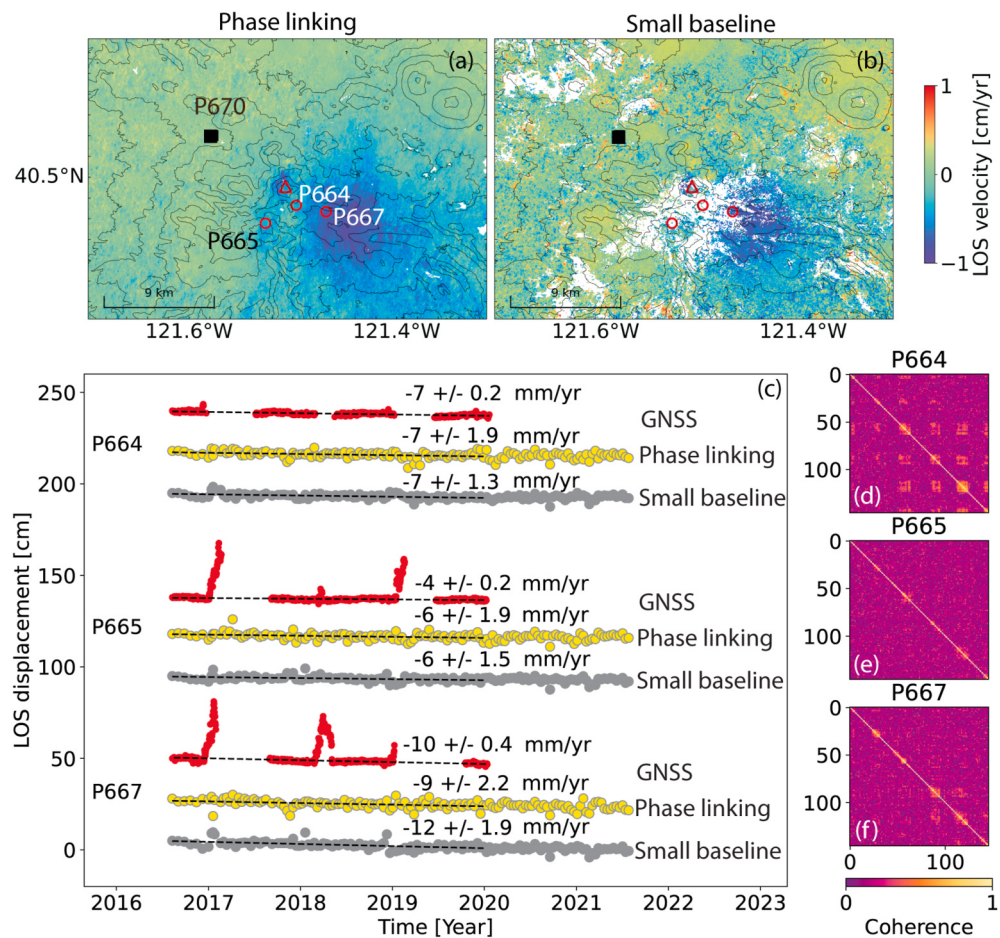


Fig. 11. Same as Fig. 10 but for Mount Lassen, California, and for continuous GNSS stations P664, P665 and P667. Reference points: GNSS station P670. Red triangle: volcano peak. (For interpretation of the references to color in this figure legend, the reader is referred to the Web version of this article.)

unwrap errors don't propagate, suggesting that the combined phase linking has advantages retrieving the signal compared to GNSS (Fig. 11c). Comparing GNSS displacements for the three stations after filtering outliers with InSAR observations obtained from both phase linking and small baseline, indicate that they agree with each other, and the differences fall within standard deviation.

6.3. Three Sisters volcanoes

The Three Sisters volcanoes are very challenging targets for InSAR because strong seasonal decorrelation hampers phase-unwrapping and long temporal baseline interferograms are decorrelated. The coherence matrices show that the temporal coherence behavior in the area varies between light seasonal decorrelation (Fig. 12e), strong seasonal decorrelation (Fig. 12f), and long-term decorrelated (Fig. 12d). However, the coherent scatterers are surrounded by low coherent and decorrelated regions which contaminate them during unwrapping. Hence the single-reference network is not a good option for unwrapping as we discussed in section 4. For seasonal unwrap errors the simulation in section 4 suggests the inversion of a Delaunay network using L1-norm minimization (Fig. 3c). The LOS velocity map obtained from the Delaunay network inverted using L1-norm is shown in Fig. 12a (the velocity map obtained from L2-norm minimization of Delaunay network is shown in supplementary Figure S3.3 in which we observe inconsistencies around the volcanoes in the lower left most likely caused by unwrapping errors). We show displacement time-series from both L1-and L2-norm minimizations for three stations including GNSS station HUSB in Fig. 12b. Both InSAR and GNSS data are referenced to the GNSS station BEND. The L1-

norm displacement time-series suggests 1.15 cm displacement for the pixel of GNSS station HUSB since late 2020 (from the difference of displacement in June 2020 and March 2022) with a rate of $6 \pm 2.7 \text{ mm/yr}$ which is slightly lower than GNSS data ($\sim 1 \text{ cm/yr}$). This shows that phase linking followed by the L1-norm minimization of a Delaunay unwrapping network can potentially provide displacement data even in cases of strong seasonal decorrelation. This signal, however, is very localized and does not support the renewed inflation of the well-known magmatic source west of South Sister volcano (Lisowski et al., 2021; Wicks et al., 2002).

6.4. Mud Creek landslide

LOS velocities from the combined phase linking and small baseline approaches for the period from 2015 to May 2017 (Fig. 13 a, b) prior to the May 20th, 2017 Mud Creek landslide (marked by a red solid line in Fig. 13c) demonstrate the higher spatial resolution of the phase linking approach compared to the standard small baseline approach (7 azimuth looks and 19 range looks, sequential network with 5 connections, temporal coherence threshold of 0.7). The persistent scatterers are shown in Fig. 13c and the combined PS and DS map in Fig. 13b. Handwerger et al. (2019) presented higher spatial resolution classic small baseline data (1 azimuth look, 2 range looks) but they manually selected the individual interferograms of the network. The LOS displacement time-series for point P0 shows movements of -3.8 cm/yr before February 2016 and an increase in the velocity up to -6.2 cm/yr from February 2016 until May 2017 (Fig. 13d), similar to the results of Handwerger et al. (2019) who attribute the increase in velocity to an increase in rainfall.

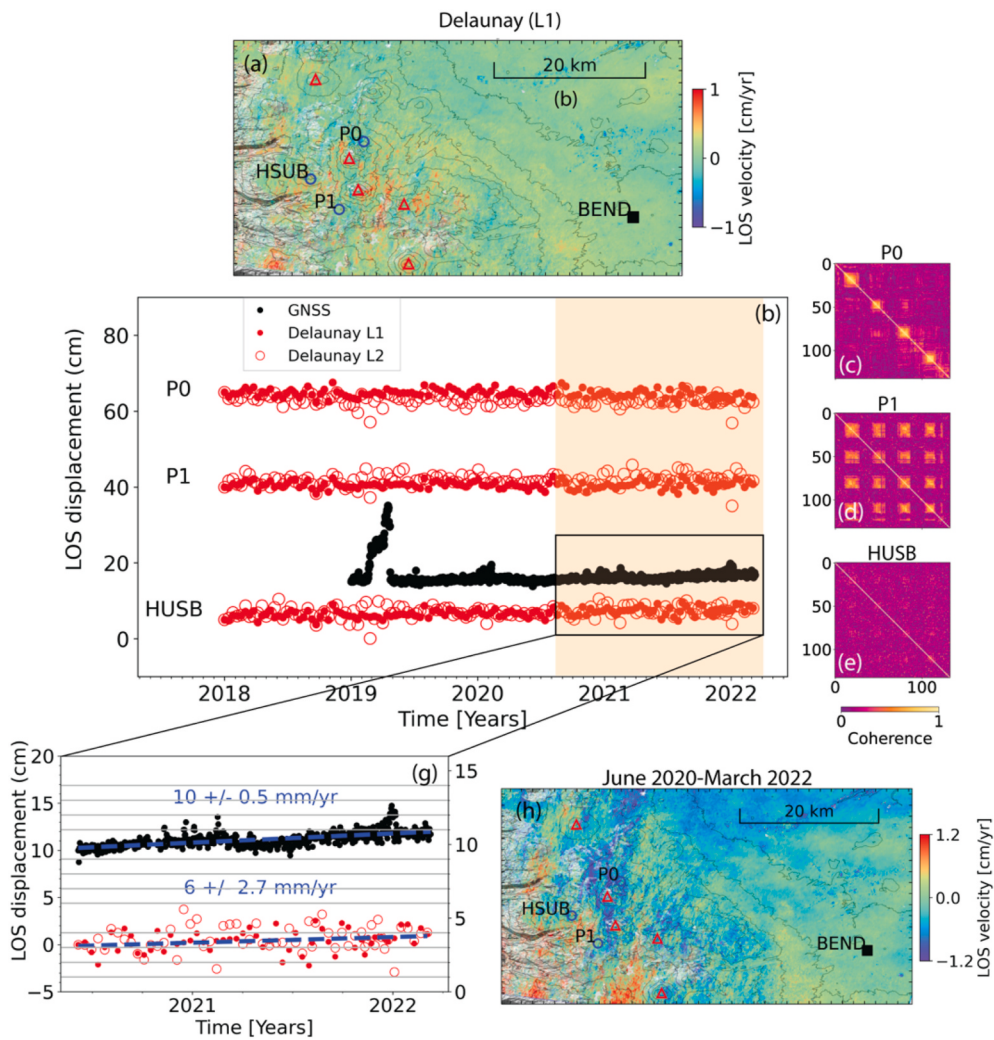


Fig. 12. (a) LOS velocity obtained from phase linking using Delaunay unwrapping networks inverted with L1-norm minimization. (c) LOS displacement time-series for points P0, P1 and GNSS station HUSB. Black dots: GNSS observations converted to LOS direction. Red dots and circles: LOS displacement time-series after inversion of Delaunay network using L1-and L2-norm minimizations respectively. Both GNSS and InSAR observations are referenced to station BEND marked by black square in (a, b). (d-f) Coherence matrix for points HUSB, P1 and P0. (g) Displacement time-series for station HUSB and h) LOS velocity for June 2020 to March 2022 period. (For interpretation of the references to color in this figure legend, the reader is referred to the Web version of this article.)

6.5. Miami Beach urban infrastructure

We use 2016–2021 data of the northern Miami Beach island, Florida, (Fig. 14a), to demonstrate the PS identification capability of MiaplPy and that it can monitor urban infrastructure. We use a SRTM DEM (Farr et al., 2007) with a resolution of 30 m for topographic phase residual correction. The LOS velocity map for the PS (Fig. 14b) and for the joint PS and DS (Fig. 14c) shows several areas with averaged LOS velocities of $\sim 0.6 \text{ cm/yr}$.

A zoom-in for one of the subsiding areas shows the locations of the PS and DS pixels on and around a 12-story coastal high-rise which was completed in 2016 (Fig. 15). Up to 2 cm LOS displacement occurred until 2018 and since then it continues at rates up to 3.2 mm/yr (Fig. 15d). A local reference point reduces the noise related to residual tropospheric phase variation. As the SRTM digital elevation model does not contain the correct scatterer heights in urban areas the geolocation correction has been applied (additional subsiding buildings are shown in the supplementary section S3D).

The geolocation correction is illustrated in Fig. 16. Some of the PS pixels have a DEM error of $\sim 40 \text{ m}$ (red colors), indicating that these PS are located on the roof of the high-rises. For these pixels the SRTM DEM has an elevation of $7 - 12 \text{ m}$ leading to geolocations at less horizontal distance to the satellite than the high-rises (Fig. 16b). The geolocation correction places these pixels within the footprint of the high-rise.

A plot of the estimated elevations versus the DSM elevations (Fig. 16e) shows that for some pixels the two elevations are different.

There are pixels with $40 - 50 \text{ m}$ DSM elevation (inside the building footprints, encircled by a dashed line in Fig. 16e) but $0 - 20 \text{ m}$ estimated elevation, as well as pixels with $0 - 20 \text{ m}$ DSM elevation (outside the building footprints) and $40 - 50 \text{ m}$ estimated elevations. There are three reasons for these discrepancies. First, within the building footprints the signal can be scattered from the rooftop as well as from lower levels including the base of the building (B1, B2', B3 in Fig. 16f). Second, as we use the center of a pixel, the DSM elevation does not necessarily represent the scatterer, for example for radar pixels that include both, the base as well as the roof of a high-rise. Third, the uncertainty of the estimated DEM error can lead to pixel dislocations. Fig. 16f also illustrates layover in an urban environment, scatterers B1 and B1'' have the same radar range although they are at different locations.

The uncertainty of the DEM error for the geolocation correction is assessed in Fig. 17 as a function of different numbers of images. We simulate the topographic phase of a 60 m high-rise using the baseline history of the Sentinel-1 Miami images, add a Gaussian phase noise with zero mean and 4.5 rad standard deviation equivalent to 2 cm , and invert for the height using least squares. For 130 images and 100 realizations, the standard deviation for height retrieval is 5.4 m and the resulting horizontal dislocation by assuming an incidence angle of 44° degrees, is 5.6 m .

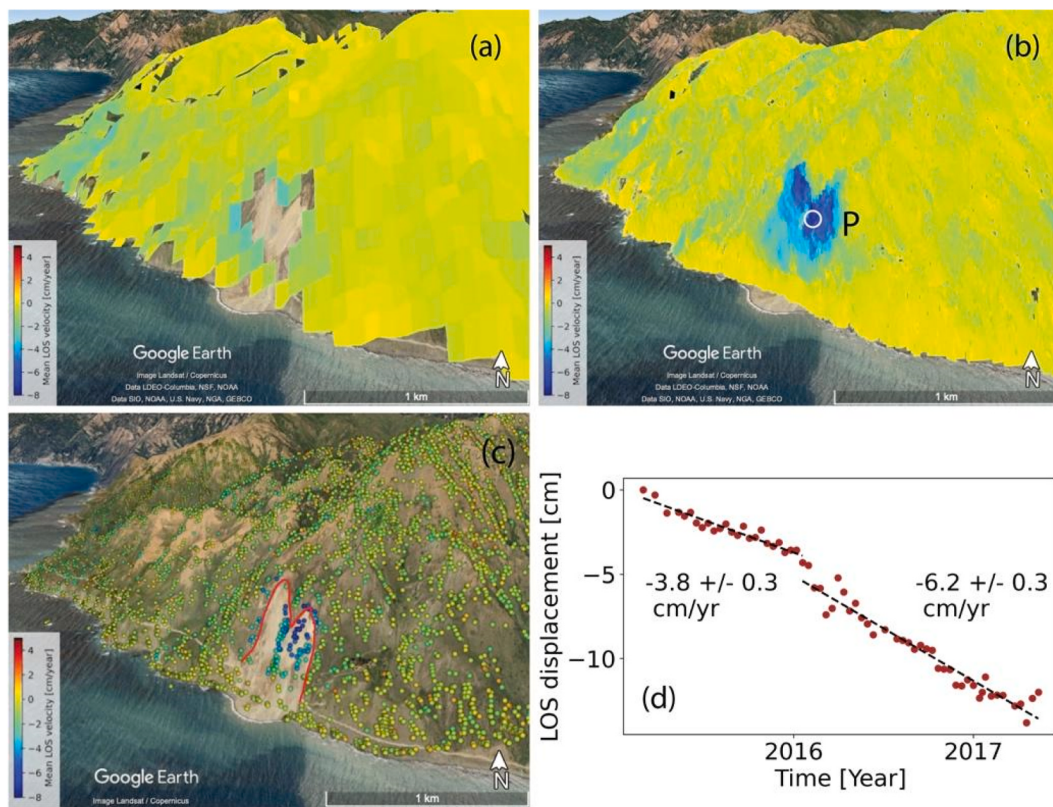


Fig. 13. LOS velocity map of Mud Creek landslide. (a) Velocity map obtained from the small baseline method with 5 sequential interferograms and (b) from sequential EMI. (c) The persistent scatterers with the landslide scarp marked by the red line. (d) Time-series of point P marked by white circle in (b). (For interpretation of the references to color in this figure legend, the reader is referred to the Web version of this article.)

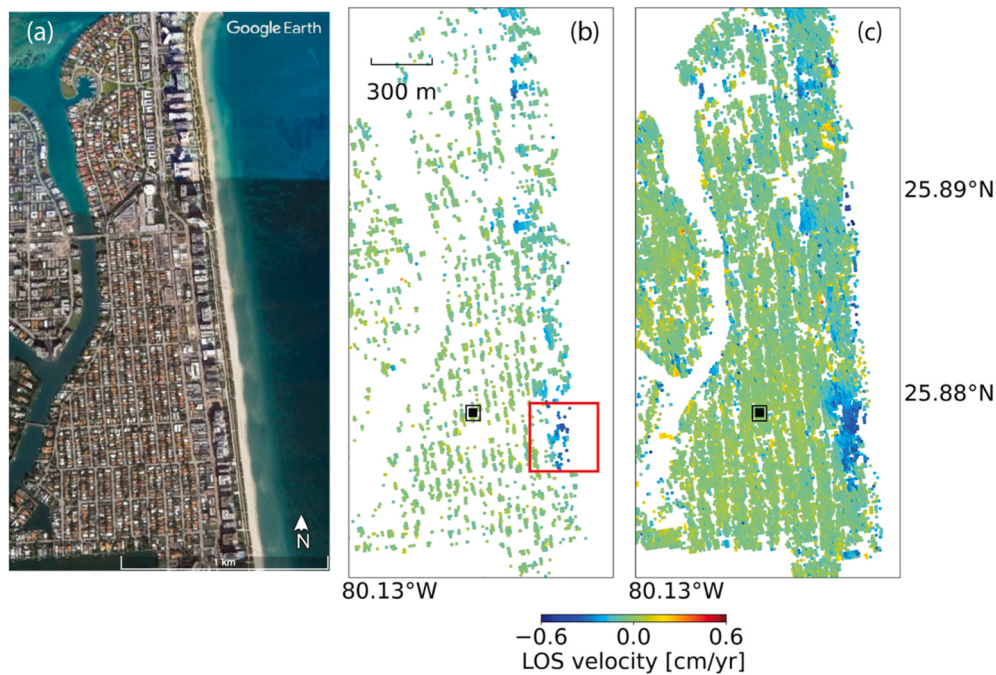


Fig. 14. (a) Optical image from Google Earth of Northern Miami Beach Island, (b) PS velocities, (c) joint PS and DS velocities. Black square: reference pixel. Rectangle refers to Fig. 15. Assuming displacements are vertical, 1 cm/yr LOS velocity corresponds to 1.39 cm/yr vertical velocity because the radar incidence angle is 44° from the vertical.

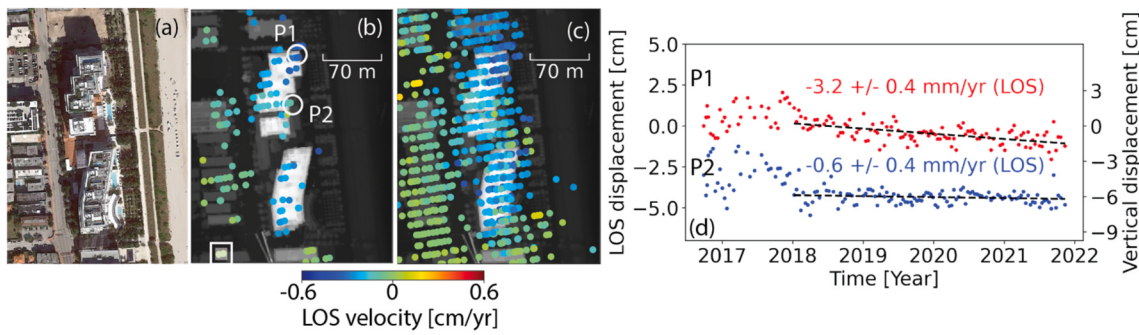


Fig. 15. Subsidence of a coastal high-rise. (a) Optical image from Google Earth. (b) PS LOS velocity superimposed on LiDAR DSM (OCM Partners, 2018). (c) Similar to (b) but with PS and DS jointly (d) Displacement time-series of points P1 and P2 marked in (b). White square on (b): reference point.

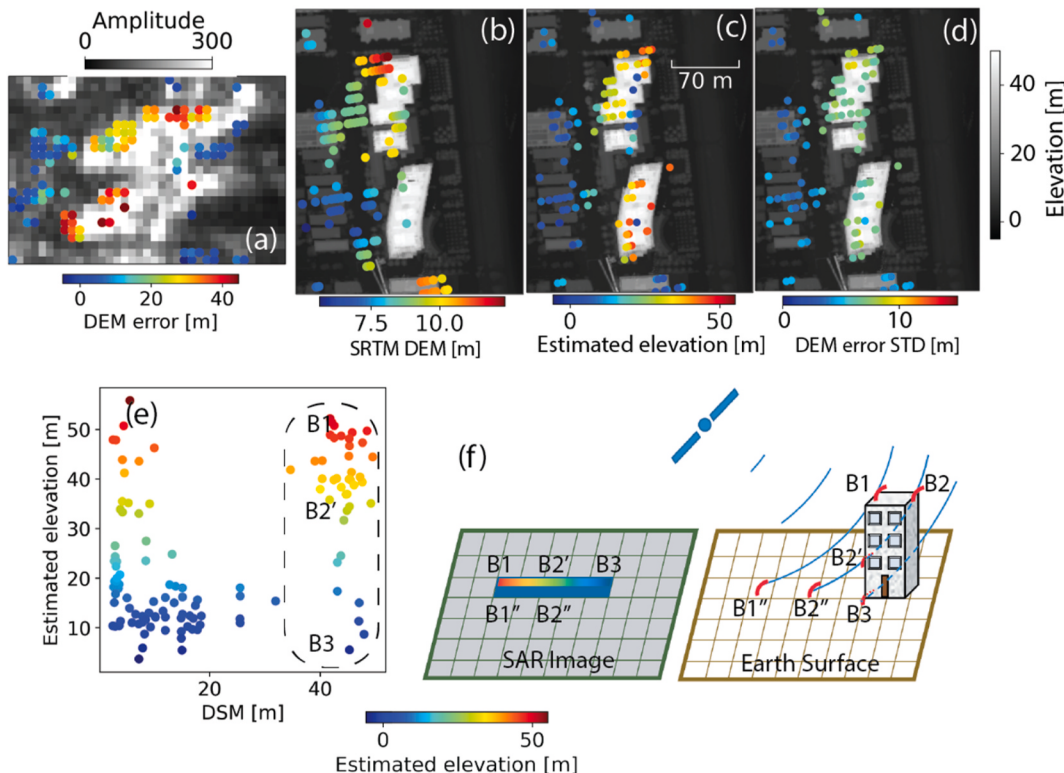


Fig. 16. (a) DEM error superimposed on average amplitude of SAR images. (b) SRTM DEM elevation without geolocation correction. (c) Estimated elevation and (d) DEM error standard deviation after geolocation correction using the DEM error. (e) The estimated elevation (SRTM DEM + DEM error) versus the LiDAR DSM elevation for the center of the PS pixels shown. (f) Cartoon showing how the scatterers on a high-rise map into SAR coordinates and the elevation of scatterers at the rooftop (B1, B2) to the bottom (B3) of the building. Dashed line in (e) encircles the scatterer on the two buildings.

7. Discussion

7.1. Systematic bias due to temporally inconsistent processes

To quantify the contribution of inconsistent short-lived processes to the displacement as a systematic bias, we add a decaying signal term to our simulation of the complex interferometric coherence matrix (eq. (9)):

$$\text{Decaying signal} = \gamma_f \exp\left(-\frac{|\Delta t|}{\tau_f}\right) \exp\left(j\nu_f \Delta t \frac{4\pi}{365\lambda}\right) \quad (13)$$

where γ_f is the short-term decaying coherence, τ_f indicates the temporal decorrelation days and ν_f is the signal velocity. We use $\gamma_f = 0.18$, $\tau_f = 11$ days, $\nu_f = 50$ mm/yr to resemble the model of De Zan., (2020). We assess the difference of mean RMSE obtained from the displacement

time-series for the four temporal coherence models of section 3 for seven different phase linking methods with and without decaying signal (Stems and bars in Fig. 18a, respectively).

For light and strong seasonal decorrelation models, short bandwidth method (pink bars) indicates an RMSE higher than 1.4 rad without and with the decaying signal (bars and stems, respectively), therefore it is not a good estimator for seasonal decorrelation. For the long-term coherent and long-term decorrelated models, using the short bandwidth method, the RMSE is 0.56 ± 0.35 rad and 0.43 ± 0.26 rad higher with decaying signal compared to without decaying signal (Fig. 18b). In comparison, the phase linking methods with full coherence matrices (all except short bandwidth) are not affected by the decaying signal as much as the short bandwidth method. The average difference of RMSE in these methods with and without the decaying signal is 0.08 ± 0.04 rad for the long-term decorrelated model and negligible (0.02 ± 0.02 rad) for the other three temporal coherence models.

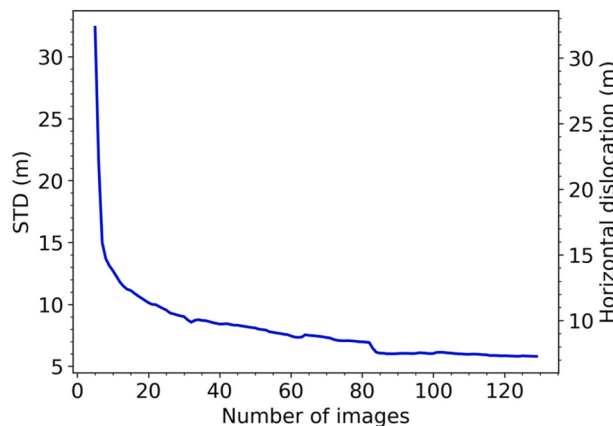


Fig. 17. The standard deviation of DEM error calculated as a function of the number of images using Sentinel-1 geometry.

Data for Bristol Dry Lake in California, an area known to exhibit a systematic bias in the short baseline approach (Zheng et al., 2022), demonstrates the effectiveness of phase linking with MiaplPy to remove systematic bias and to correct for non-zero closure phases.

Velocity maps obtained from (i) the full resolution phase linking approach inverted using sequential unwrapping networks with 1, 3 and 5 connections, and (ii) from multi-looked interferograms using the small baseline approach are depicted in Fig. 19a, b, c and Fig. 19d, e, f, respectively. The small baseline estimated velocities show a displacement signal (a systematic bias) south of the southernmost corner of the lake which decays with increasing number of connections. This area does not show any displacements using the phase linking approach. However, the phase linking estimated velocities contain a salt-and-pepper-type noise which decreases with more redundancy and is absent on the single-reference network estimated velocity (Fig. 19g). This noise is the result of local phase-unwrapping errors for one or a few pixels which are common at full resolution but not after multi-looking. They decrease in magnitude when increasing the number of

connections (see section 4). The example in supplementary section S1E, also shows the bias caused by unwrapping error propagation after phase linking that could be misinterpreted as systematic displacement bias from non-zero closure phase.

7.2. PS selection

In phase linking, the first criterion to select PS pixels is based on the number of self-similar neighbors in which the default is pixels with 10 or fewer self-similar neighbors. This number (threshold) is chosen depending on the spatial resolution of the data (Ferretti et al., 2011) with more pixels for higher resolution. Using Sentinel-1 data of Miami, a statistical analysis on the PS pixels having a high temporal coherence (greater than 0.98) shows that 95% of them have 10 or less number of self-similar neighbors (Fig. 20).

8. Conclusions

The non-linear phase linking approach implemented in the MiaplPy software addresses the main drawbacks of common small baseline and persistent scatterer InSAR techniques. First it provides spatial detail by multi-looking only self-similar neighbors and by inverting DS pixels in full spatial resolution and integrating with PS pixels. Second, it reduces the amount of non-zero closure phase at DS pixels by using all possible interferometric pairs on the fly through a full coherence matrix estimation. The software provides various choices of unwrapping networks including L1-norm minimization that leads to more robust displacement time-series depending on the temporal coherence behavior and the distribution of unwrapping errors. Sequential phase linking algorithms and parallel processing provide computational efficiency.

The workflow of the MiaplPy software consists of several steps to detect PS pixels and phase link the DS pixels to estimate wrapped phase time-series for persistent and distributed scatterers. The workflow continues with unwrapping and inverting a network of unwrapped interferograms to estimate the unwrapped time-series. The conclusions from our analysis of simulated and real data are:

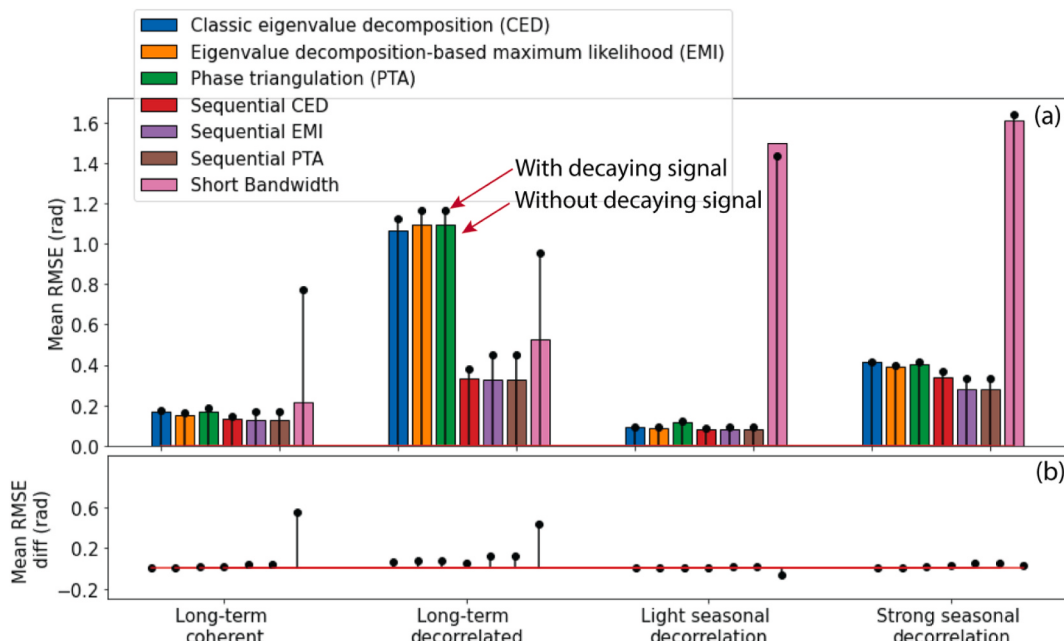


Fig. 18. Assessment of decorrelation and decaying signal contribution using the mean of root mean square error calculated for different phase linking methods. (a) Four temporal coherence models with different colors as different phase linking methods. Stem plots for each bar indicate the corresponding model with decaying signal. (b) The differences of the mean RMSE for the retrieved displacement with and without the decaying signal. (For interpretation of the references to color in this figure legend, the reader is referred to the Web version of this article.)

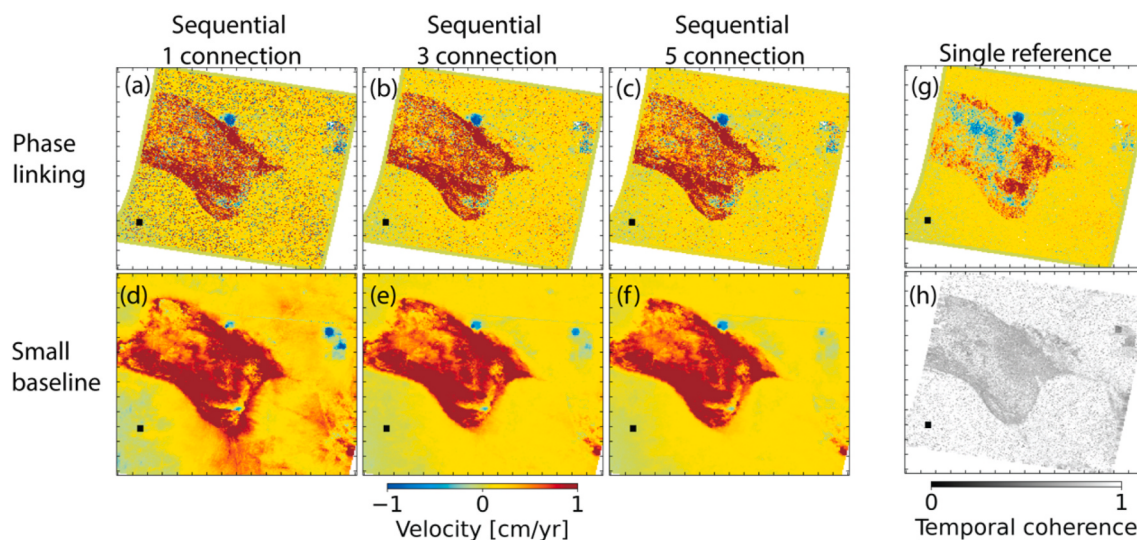


Fig. 19. Systematic bias corrected by phase linking using full coherence matrix. (a–c) Velocity maps obtained from phase linking after inverting unwrapped sequential networks with 1, 3 and 5 connections respectively. (d–f) The velocity maps obtained from the small baseline approach based on unwrapped multi-looked interferograms in sequential networks with 1, 3 and 5 connections respectively. (g) Velocity map obtained from phase linking unwrapped for single-reference interferograms. (h) Temporal coherence obtained from phase linking.

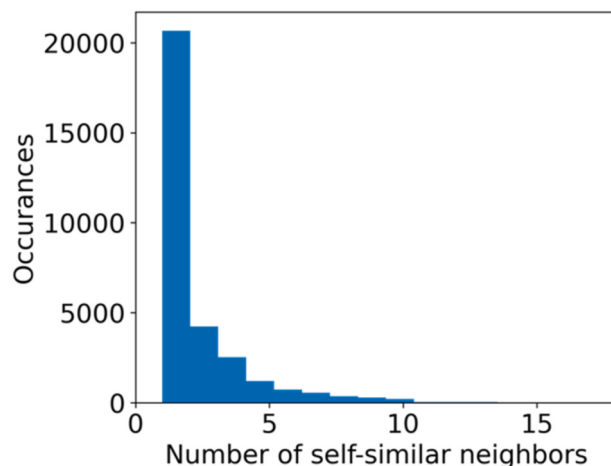


Fig. 20. Histogram of number of self-similar neighbors for scatterers with a temporal coherence greater than 0.98 using Miami data.

1. For realistic simulations where the interferometric phase contains short-lived signals, for different temporal decorrelation scenarios, using only short temporal interferograms results in larger residuals between simulated and estimated displacement in comparison to using the full complex coherence matrix for phase linking. The sequential phase linking algorithm improves accuracy and computational performance and has the ability to perform InSAR measurements over seasonally decorrelated targets.
2. Unwrapping errors propagate differently depending on the design of the unwrapping network and the inversion technique. For a single-reference network, the unwrapping errors do not propagate because the network inversion is a determined system. However, for over-determined networks unwrap error propagation compromises the accuracy of the final displacement time-series, in particular for sequential networks with few connections.
3. We make the following recommendations for unwrapping network selection depending on the temporal coherence behavior and the expected unwrap errors: (i) For cases with long-term coherent interferograms use a single-reference network (Guagua Pichincha example, Fig. 10) because the unwrap errors don't propagate and

because it requires the least memory. (ii) For cases where correlation is lost rapidly with time (long-term decorrelated) use a Delaunay network. A sufficiently redundant sequential network (>8 connections) also provides a robust solution, but memory requirements are high. L1 norm minimization is less sensitive to phase-unwrapping errors compared to L2 norm minimization but is computationally an order of magnitude more expensive. (iii) For cases with strong seasonal decorrelation and a large percentage of unwrapping errors use a Delaunay network with L1-norm minimization (Three Sisters volcanoes example, Fig. 12), but at increased computational costs.

4. The phase linking analysis implemented in the software significantly reduces the systematic bias caused by non-zero closure phase as demonstrated by simulated and real data. The software also improves interferometric coherence by de-speckling with self-similar pixels and increases the density of detected scatterers by a full resolution analysis.
5. The software also serves to identify persistent scatterers. We have demonstrated the PS monitoring capability with a case study of high-rise construction-induced land subsidence in Miami Beach island.

Authorship contribution statement

Sara Mirzaee and Heresh Fattahi developed the mathematical scope. Sara Mirzaee developed the software. Sara Mirzaee, Heresh Fattahi and Falk Amelung tested the software and processed the data. Sara Mirzaee wrote the manuscript with the help of Falk Amelung and Heresh Fattahi. Falk Amelung supervised the project.

Code availability section

The presented workflow is implemented as the Miami phase linking software in PYthon (MiaplPy), with open-source code, documentation, tutorials in Jupyter Notebook and test data freely available on GitHub (<https://github.com/insarlab/MiaplPy>) under GNU Generic Public License version 3. Figures in this manuscript are plotted using Jupyter Notebooks available at https://github.com/mirzaees/2022_MiaplPy_Mirzaee_Amelung_Fattahi. See supplementary section S3 for a technical software guide.

Declaration of competing interest

The authors declare that they have no known competing financial interests or personal relationships that could have appeared to influence the work reported in this paper.

Data availability

I have shared the link to my data/code in the code availability section of the manuscript

Acknowledgments

The Sentinel-1 data was provided by ESA and obtained from Alaska Satellite Facility (ASF) via the Seamless SAR Archive (SSARA), a service provided by the UNAVCO facility. GNSS data was provided by the University of Nevada, Reno. We thank Yunjun Zhang for discussions and guidance on code adaptation to MintPy. For computations we used systems of the Extreme Science and Engineering Discovery Environment (XSEDE) and the Frontera project of the Texas Advanced Computing Center (TAAC) which is supported by National Science Foundation grant number ACI-1548562 and OAC-1818253. We thank Si Liu at TACC for HPC advice. This research was supported by NASA awards to F.A. (Grant No. NNX16AK52G, NNX14AL39G). Part of the research was carried out at the Jet Propulsion Laboratory, California Institute of Technology, under a contract with the National Aeronautics and Space Administration with support provided from the OPERA (Observational Products for End-users from Remote sensing Analysis) project.

Appendix A. Supplementary data

Supplementary data to this article can be found online at <https://doi.org/10.1016/j.cageo.2022.105291>.

References

- Agram, P.S., Jolivet, R., Riel, B., Lin, Y.N., Simons, M., Hetland, E., Doin, M.-P., Lasserre, C., 2013. New radar interferometric time series analysis toolbox released. *Eos, Transactions American Geophysical Union* 94, 69–70. <https://doi.org/10.1029/2013EO070001>.
- Amelung, F., Jonsson, S., Zebker, H., Segall, P., 2000. Widespread uplift and “trapdoor” faulting on Galapagos volcanoes observed with radar interferometry. *Nature* 407, 993–996. <https://doi.org/10.1038/35039604>.
- Ansari, H., de Zan, F., Bamler, R., 2018. Efficient phase estimation for interferogram stacks. *IEEE Trans. Geosci. Rem. Sens.* 56, 4109–4125. <https://doi.org/10.1109/TGRS.2018.2826045>.
- Ansari, H., de Zan, F., Bamler, R., 2017. Sequential estimator: toward efficient InSAR time series analysis. *IEEE Trans. Geosci. Rem. Sens.* 55, 5637–5652. <https://doi.org/10.1109/TGRS.2017.2711037>.
- Ansari, H., de Zan, F., Parizzi, A., 2021. Study of systematic bias in measuring surface deformation with SAR interferometry. *IEEE Trans. Geosci. Rem. Sens.* 59, 1285–1301. <https://doi.org/10.1109/TGRS.2020.3003421>.
- Arnold, D.W.D., Biggs, J., Wadge, G., Mothes, P., 2018. Using satellite radar amplitude imaging for monitoring syn-eruptive changes in surface morphology at an ice-capped stratovolcano. *Remote Sens. Environ.* 209, 480–488. <https://doi.org/10.1016/j.rse.2018.02.040>.
- Berardino, P., Fornaro, G., Lanari, R., Sansosti, E., 2002. A new algorithm for surface deformation monitoring based on small baseline differential SAR interferograms. *IEEE Trans. Geosci. Rem. Sens.* 40, 2375–2383. <https://doi.org/10.1109/TGRS.2002.803792>.
- Blewitt, G., Hammond, W., Kreemer, C., 2018. Harnessing the GPS Data Explosion for Interdisciplinary Science, 99. *Eos, Washington DC*. <https://doi.org/10.1029/2018EO104623>.
- Cao, N., Lee, H., Jung, H.C., 2016. A phase-decomposition-based PSInSAR processing method. *IEEE Trans. Geosci. Rem. Sens.* 54, 1074–1090. <https://doi.org/10.1109/TGRS.2015.2473818>.
- Chaussard, E., Amelung, F., Abidin, H., Hong, S.-H., 2013. Sinking cities in Indonesia: ALOS PALSAR detects rapid subsidence due to groundwater and gas extraction. *Remote Sens. Environ.* 128, 150–161. <https://doi.org/10.1016/j.rse.2012.10.015>.
- Chen, C.W., Zebker, H.A., 2002. Phase unwrapping for large SAR interferograms: statistical segmentation and generalized network models. *IEEE Trans. Geosci. Rem. Sens.* 40, 1709–1719. <https://doi.org/10.1109/TGRS.2002.802453>.
- Chen, C.W., Zebker, H.A., 2001. Two-dimensional phase unwrapping with use of statistical models for cost functions in nonlinear optimization. *J. Optical Soc. Am. A* 18, 338. <https://doi.org/10.1364/josaa.18.000338>.
- Chen, C.W., Zebker, H.A., 2000. Network approaches to two-dimensional phase unwrapping: intractability and two new algorithms. *J. Optical Soc. Am. A* 17, 401. <https://doi.org/10.1364/JOSAA.17.000401>.
- Colesanti, C., Ferretti, A., Prati, C., Rocca, F., 2003. Monitoring landslides and tectonic motions with the permanent scatterers technique. *Eng. Geol.* 68, 3–14. [https://doi.org/10.1016/S0013-7952\(02\)00195-3](https://doi.org/10.1016/S0013-7952(02)00195-3).
- Constantini, M., Malvarosa, F., Minati, F., Pietranera, L., Milillo, G., 2002. A three-dimensional phase unwrapping algorithm for processing of multitemporal SAR interferometric measurements. *Int. Geosci. Remote Sens. Symp. (IGARSS) 3*, 1741–1743. <https://doi.org/10.1109/igarss.2002.1026239>.
- de Luca, C., Casu, F., Manunta, M., Onorato, G., Lanari, R., 2022. Comments on “study of systematic bias in measuring surface deformation with SAR interferometry”. *IEEE Trans. Geosci. Rem. Sens.* 60, 1–5. <https://doi.org/10.1109/TGRS.2021.3103037>.
- de Zan, F., 2020. Progressive InSAR phase estimation. *Electr. Eng. Syst. Sci.* 3–7. <https://doi.org/10.48550/arXiv.2010.02533>.
- de Zan, F., López-Dekker, P., 2011. SAR image stacking for the exploitation of long-term coherent targets. *Geosci. Rem. Sens. Lett. IEEE* 8, 502–506. <https://doi.org/10.1109/LGRS.2010.2089494>.
- de Zan, F., Rocca, F., 2005. Coherent processing of long series of SAR images. *Int. Geosci. Remote Sens. Symp. (IGARSS) 3*, 1987–1990. <https://doi.org/10.1109/IGARSS.2005.1526402>.
- Derrick, B., Toher, D., White, P., 2017. How to compare the means of two samples that include paired observations and independent observations: a companion to Derrick, Russ, Toher and White (2017). *Quant. Method Psychol.* 13, 120–126. <https://doi.org/10.20982/tqmp.13.2.p120>.
- Even, M., Schulz, K., 2018. InSAR deformation analysis with distributed scatterers: a review complemented by new advances. *Remote Sens. (Basel)* 10, 744. <https://doi.org/10.3390/rs10050744>.
- Farr, T.G., Rosen, P.A., Caro, E., Crippen, R., Duren, R., Hensley, S., Kobrick, M., Paller, M., Rodriguez, E., Roth, L., Seal, D., Shaffer, S., Shimada, J., Umland, J., Werner, M., Oskin, M., Burbank, D., Alsdorf, D., 2007. The shuttle radar topography mission. *Rev. Geophys.* 45, RG2004. <https://doi.org/10.1029/2005RG000183>.
- Fattahai, H., Agram, P., Simons, M., 2017. A network-based enhanced spectral diversity approach for TOPS time-series analysis. *IEEE Trans. Geosci. Rem. Sens.* 55, 777–786. <https://doi.org/10.1109/TGRS.2016.2614925>.
- Fattahai, H., Amelung, F., 2016. InSAR observations of strain accumulation and fault creep along the Chaman Fault system, Pakistan and Afghanistan. *Geophys. Res. Lett.* 43, 8399–8406. <https://doi.org/10.1002/2016GL070121>.
- Fattahai, H., Amelung, F., 2013. DEM error correction in InSAR time series. *IEEE Trans. Geosci. Rem. Sens.* 51, 4249–4259. <https://doi.org/10.1109/TGRS.2012.2227761>.
- Ferretti, A., Fumagalli, A., Novali, F., Prati, C., Rocca, F., Rucci, A., 2011. A new algorithm for processing interferometric data-stacks: SqueeSAR. *IEEE Trans. Geosci. Rem. Sens.* 49, 3460–3470. <https://doi.org/10.1109/TGRS.2011.2124465>.
- Ferretti, A., Prati, C., Rocca, F., 2001. Permanent scatterers in SAR interferometry. *IEEE Trans. Geosci. Rem. Sens.* 39, 8–20. <https://doi.org/10.1109/36.898661>.
- Ferretti, A., Prati, C., Rocca, F., 2000. Nonlinear subsidence rate estimation using permanent scatterers in differential SAR interferometry. *IEEE Trans. Geosci. Rem. Sens.* 38, 2202–2212. <https://doi.org/10.1109/36.868878>.
- Fornaro, G., Verde, S., Reale, D., Paucullo, A., 2015. CAESAR: an approach based on covariance matrix decomposition to improve multibaseline-multitemporal interferometric SAR processing. *IEEE Trans. Geosci. Rem. Sens.* 53, 2050–2065. <https://doi.org/10.1109/TGRS.2014.2352853>.
- Funning, G.J., Parsons, B., Wright, T.J., Jackson, J.A., Fielding, E.J., 2005. Surface displacements and source parameters of the 2003 Bam (Iran) earthquake from Envisat advanced synthetic aperture radar imagery. *J. Geophys. Res. Solid Earth* 110, 1–23. <https://doi.org/10.1029/2004JB003338>.
- Guarnieri, A.M., Tebaldini, S., 2008. On the exploitation of target statistics for SAR interferometry applications. *IEEE Trans. Geosci. Rem. Sens.* 46, 3436–3443. <https://doi.org/10.1109/TGRS.2008.2001756>.
- Guarnieri, A.M., Tebaldini, S., 2007. Hybrid Cramér-Rao bounds for crustal displacement field estimators in SAR interferometry. *IEEE Signal Process. Lett.* 14, 1012–1015. <https://doi.org/10.1109/LSP.2007.904705>.
- Handwerger, A.L., Huang, M.H., Fielding, E.J., Booth, A.M., Bürgmann, R., 2019. A shift from drought to extreme rainfall drives a stable landslide to catastrophic failure. *Sci. Rep.* 9, 1–12. <https://doi.org/10.1038/s41598-018-38300-0>.
- Hoffmann, J., Zebker, H.A., Galloway, D.L., Amelung, F., 2001. Seasonal subsidence and rebound in Las Vegas Valley, Nevada, observed by synthetic aperture radar interferometry. *Water Resour. Res.* 37, 1551–1566. <https://doi.org/10.1029/2000WR900404>.
- Hoffmann, L., Günther, G., Li, D., Stein, O., Wu, X., Griessbach, S., Heng, Y., Konopka, P., Müller, R., Vogel, B., Wright, J.S., 2019. From ERA-Interim to ERA5: the considerable impact of ECMWF’s next-generation reanalysis on Lagrangian transport simulations. *Atmos. Chem. Phys.* 19, 3097–3214. <https://doi.org/10.5194/acp-19-3097-2019>.
- Hooper, A., 2008. A multi-temporal InSAR method incorporating both persistent scatterer and small baseline approaches. *Geophys. Res. Lett.* 35, L16302. <https://doi.org/10.1029/2008GL034654>.
- Hooper, A., Segall, P., Zebker, H., 2007. Persistent scatterer interferometric synthetic aperture radar for crustal deformation analysis, with application to Volcan Alcedo, Galapagos. *J. Geophys. Res.* 112, B07407. <https://doi.org/10.1029/2006JB004763>.
- Hooper, A., Zebker, H., Segall, P., Kampes, B., 2004. A new method for measuring deformation on Volcanoes and other natural terrains using InSAR Persistent Scatterers. *Geophys. Res. Lett.* 31, 1–5. <https://doi.org/10.1016/j.jgtec.2011.10.013>.

- Hoyle, D.C., Rattray, M., 2004. Principal-component-analysis eigenvalue spectra from data with symmetry-breaking structure. *Phys. Rev. E - Stat. Nonlinear Soft Matter Phys.* 69 <https://doi.org/10.1103/PhysRevE.69.026124>.
- Jolivet, R., Agram, P.S., Lin, N.Y., Simons, M., Doin, M., Peltzer, G., Li, Z., 2014. Journal of geophysical research : solid Earth improving InSAR geodesy using global atmospheric models. *J. Geophys. Res. Solid Earth* 119, 2324–2341. <https://doi.org/10.1002/2013JB010588>.Received.
- Jolivet, R., Grandin, R., Lasserre, C., Doin, M.P., Peltzer, G., 2011. Systematic InSAR tropospheric phase delay corrections from global meteorological reanalysis data. *Geophys. Res. Lett.* 38, 1–6. <https://doi.org/10.1029/2011GL048757>.
- Joughin, I., Smith, B.E., Abdalati, W., 2011. Glaciological advances made with interferometric synthetic aperture radar. *J. Glaciol.* <https://doi.org/10.3189/002214311796406158>.
- Jung, J., Kim, D., Palanisamy Vadivel, S.K., Yun, S.-H., 2019. Long-term deflection monitoring for bridges using X and C-band time-series SAR interferometry. *Remote Sens. (Basel)* 11, 1258. <https://doi.org/10.3390/rs11111258>.
- Kumar, V., Venkataraman, G., 2011. SAR interferometric coherence analysis for snow cover mapping in the western Himalayan region. *Int. J. Digit Earth* 4, 78–90. <https://doi.org/10.1080/17538940903521591>.
- Lanari, R., Casu, F., Manzo, M., Lundgren, P., 2007. Application of the SBAS-DInSAR technique to fault creep: a case study of the Hayward fault, California. *Remote Sens. Environ.* 109, 20–28. <https://doi.org/10.1016/j.rse.2006.12.003>.
- Lanari, R., Mora, O., Manunta, M., Mallorquí, J.J., Berardino, P., Sansosti, E., 2004. A small-baseline approach for investigating deformations on full-resolution differential SAR interferograms. *IEEE Trans. Geosci. Rem. Sens.* 42, 1377–1386. <https://doi.org/10.1109/TGRS.2004.828196>.
- Lauknes, T.R., Dehls, J., Larsen, Y., Hogda, K.A., Weydahl, D.J., 2006. A Comparison of SBAS and PS ERS InSAR for Subsidence Monitoring in Oslo, Norway. European Space Agency, (Special Publication) ESA SP.
- Lauknes, T.R., Zebker, H.A., Larsen, Y., 2011. InSAR deformation time series using an L1-norm small-baseline approach. *IEEE Trans. Geosci. Rem. Sens.* 49, 536–546. <https://doi.org/10.1109/TGRS.2010.2051951>.
- Lisowski, M., McCaffrey, R., Wicks, C.W., Dzurisin, D., 2021. Geodetic constraints on a 25-year magmatic inflation episode near three sisters, central Oregon. *J. Geophys. Res. Solid Earth* 126, 1–21. <https://doi.org/10.1029/2021JB022360>.
- Morales Rivera, A.M., Amelung, F., Mothes, P., 2016. Volcano deformation survey over the Northern and Central Andes with ALOS InSAR time series. *G-cubed* 17, 2869–2883. <https://doi.org/10.1002/2016GC006393>.
- Moretto, S., Bozzano, F., Mazzanti, P., 2021. The role of satellite insar for landslide forecasting: limitations and openings. *Remote Sens. (Basel)* 13, 1–31. <https://doi.org/10.3390/rs13183735>.
- Morishita, Y., Lazecky, M., Wright, T.J., Weiss, J.R., Elliott, J.R., Hooper, A., 2020. LiCSBAS: an open-source insar time series analysis package integrated with the LiCSAR automated sentinel-1 InSAR processor. *Remote Sens. (Basel)* 12, 5–8. <https://doi.org/10.3390/rs12030424>.
- Motagh, M., Shamshiri, R., Haghshenas Haghighi, M., Wetzel, H.-U., Akbari, B., Nahavandchi, H., Roessner, S., Arabi, S., 2017. Quantifying groundwater exploitation induced subsidence in the Rāfsanjan plain, southeastern Iran, using InSAR time-series and in situ measurements. *Eng. Geol.* 1–18. <https://doi.org/10.1016/j.enggeo.2017.01.011>.
- Navneet, S., Kim, J.-W., Lu, Z., 2018. A new InSAR persistent scatterer selection technique using top eigenvalue of coherence matrix. *IEEE Trans. Geosci. Rem. Sens.* 56, 1969–1978. <https://doi.org/10.1109/TGRS.2017.2771386>.
- Parkinson, R.W., 2021. Speculation on the role of sea-level rise in the tragic collapse of the Surfside condominium (Miami Beach, Florida U.S.A.) was a bellwether moment for coastal zone management practitioners. *Ocean Coast Manag.* 215, 105968. <https://doi.org/10.1016/j.occoaman.2021.105968>.
- Pepe, A., Yang, Y., Manzo, M., Lanari, R., 2015. Improved EMCF-SBAS processing chain based on advanced techniques for the noise-filtering and selection of small baseline multi-look DInSAR interferograms. *IEEE Trans. Geosci. Rem. Sens.* 53, 4394–4417. <https://doi.org/10.1109/TGRS.2015.2396875>.
- Piantanida, R., Miranda, N., Hajduch, G., 2017. MPC-S1: Thermal Denoising of Products Generated by the S-1 IPF, S-1 Mission Performance Center.
- Samiee-Esfahani, S., Martins, J.E., van Leijen, F., Hanssen, R.F., 2016. Phase estimation for distributed scatterers in InSAR stacks using integer least squares estimation. *IEEE Trans. Geosci. Rem. Sens.* 54, 5671–5687. <https://doi.org/10.1109/TGRS.2016.2566604>.
- Schmidt, D.A., Bürgmann, R., 2003. Time-dependent land uplift and subsidence in the Santa Clara valley, California, from a large interferometric synthetic aperture radar data set. *J. Geophys. Res. Solid Earth* 108, 1–13. <https://doi.org/10.1029/2002jb002267>.
- Scholz, F.W., Stephens, M.A., 1987. K-sample Anderson–darling tests. *J. Am. Stat. Assoc.* 82, 918–924. <https://doi.org/10.1080/01621459.1987.10478517>.
- Shamshiri, R., Nahavandchi, H., Motagh, M., Hooper, A., 2018. Efficient ground surface displacement monitoring using Sentinel-1 data: integrating distributed scatterers (DS) identified using two-sample t-test with persistent scatterers (PS). *Remote Sens. (Basel)* 10, 1–14. <https://doi.org/10.3390/rs10050794>.
- Shanker, P., Casu, F., Zebker, H.A., Lanari, R., 2011. Comparison of persistent scatterers and small baseline time-series InSAR results: a case study of the San Francisco bay area. *Geosci. Rem. Sens. Lett. IEEE* 8, 592–596. <https://doi.org/10.1109/LGRS.2010.2095829>.
- Shanker, P., Zebker, H., 2007. Persistent scatterer selection using maximum likelihood estimation. *Geophys. Res. Lett.* 34, L22301. <https://doi.org/10.1029/2007GL030806>.
- Soja, M.J., Persson, H., Ulander, L.M.H., 2015. Estimation of forest height and canopy density from a single InSAR correlation coefficient. *Geosci. Rem. Sens. Lett. IEEE* 12, 646–650. <https://doi.org/10.1109/LGRS.2014.2354551>.
- Spaans, K., Hooper, A., 2016. InSAR processing for volcano monitoring and other near-real time applications. *J. Geophys. Res. Solid Earth* 121, 2947–2960. <https://doi.org/10.1002/2015JB012752>.
- Stephens, M.A., 1970. Use of the Kolmogorov-Smirnov, Cramer-Von Mises and related statistics without extensive tables. *J. R. Stat. Soc. Ser. B* 32, 115–122. <https://doi.org/10.1111/j.2517-6161.1970.tb00821.x>.
- Wang, J., Deng, Y., Wang, R., Ma, P., Lin, H., 2019. A small-baseline InSAR inversion algorithm combining a smoothing constraint and L1-norm minimization. *Geosci. Rem. Sens. Lett. IEEE* 16, 1061–1065. <https://doi.org/10.1109/LGRS.2019.2893422>.
- Wicks, C.W., Dzurisin, D., Ingebritsen, S., Thatcher, W., Lu, Z., Iverson, J., 2002. Magmatic activity beneath the quiescent Three Sisters volcanic center, central Oregon Cascade Range, USA. *Geophys. Res. Lett.* 29 <https://doi.org/10.1029/2001GL014205>, 26–1–26–4.
- Yunjun, Z., Fattah, H., Amelung, F., 2019. Small baseline InSAR time series analysis: unwrapping error correction and noise reduction. *Comput. Geosci.* 133, 104331. <https://doi.org/10.1016/j.cageo.2019.104331>.
- Zebker, H., Shankar, P., Hooper, A., 2007. InSAR Remote sensing over decorrelating terrains: persistent scattering methods. In: 2007 IEEE Radar Conference. IEEE, pp. 717–722. <https://doi.org/10.1109/RADAR.2007.374307>.
- Zheng, Y., Fattah, H., Agram, P., Simons, M., Rosen, P., 2022. On closure phase and systematic bias in Multilooked SAR interferometry. *IEEE Trans. Geosci. Rem. Sens.* 60, 1–11. <https://doi.org/10.1109/TGRS.2022.3167648>.